

# 15 years of VLT/UVES OH intensities and temperatures in comparison with TIMED/SABER data

Stefan Noll<sup>a,\*</sup>, Stefan Kimeswenger<sup>b,a</sup>, Bastian Proxauf<sup>a,c</sup>, Stefanie Unterguggenberger<sup>a</sup>, Wolfgang Kausch<sup>d,a</sup>, Amy M. Jones<sup>e</sup>

<sup>a</sup>*Institut für Astro- und Teilchenphysik, Universität Innsbruck, Technikerstr. 25/8, 6020 Innsbruck, Austria*

<sup>b</sup>*Instituto de Astronomía, Universidad Católica del Norte, Avenida Angamos 0610, Antofagasta, Chile*

<sup>c</sup>*Max Planck Institute for Solar System Research, Justus-von-Liebig-Weg 3, 37077 Göttingen, Germany*

<sup>d</sup>*Department of Astrophysics, University of Vienna, Türkenschanzstrasse 17, 1180 Vienna, Austria*

<sup>e</sup>*Max Planck Institute for Astrophysics, Karl-Schwarzschild-Str. 1, 85748 Garching, Germany*

---

## Abstract

The high-resolution echelle spectrograph UVES of the Very Large Telescope at Cerro Paranal in Chile has been regularly operated since April 2000. Thus, UVES archival data originally taken for astronomical projects but also including sky emission can be used to study airglow variations on a time scale longer than a solar cycle. Focusing on OH emission and observations until March 2015, we considered about 3,000 high-quality spectra from two instrumental set-ups centred on 760 and 860 nm, which cover about 380 nm each. These data allowed us to measure line intensities for several OH bands in order to derive band intensities and rotational temperatures for different upper vibrational levels as a function of solar activity and observing date. The results were compared with those derived from emission and temperature profile data of the radiometer SABER on the TIMED satellite taken in the Cerro Paranal area between 2002 and 2015. In agreement with the SABER data, the long-term variations in OH intensity and temperature derived from the UVES data are dominated by the solar cycle, whereas secular trends appear to be negligible. Combining the UVES and SABER results, the solar cycle effects for the OH intensity and temperature are about 12 to 17% and 4 to 5 K per 100 sfu and do not significantly depend on the selected OH band. The data also reveal that variations of the effective OH emission layer height and air density can cause significant changes in the OH rotational temperatures due to a varying ratio of OH thermalising collisions by air molecules and OH radiation, deactivation, and destruction processes which impede the rotational relaxation. However, this effect appears to be of minor importance for the explanation of the rotational temperature variations related to the solar activity cycle, which causes only small changes in the OH emission profile.

*Keywords:* OH emission, Spectroscopy, Temperature, Solar cycle

---

## 1. Introduction

One of the most prominent nighttime airglow emissions of the Earth's mesopause region is caused by excited hydroxyl (OH) (Meinel, 1950). It originates at a typical altitude of 87 km with a full width at half maximum (FWHM) of about 8 to 9 km (Baker and Stair, 1988). The emission is related to a reaction of atomic hydrogen and ozone (Bates and Nicolet, 1950), which mainly populates the vibrational levels  $v = 8$  and  $9$  of the OH electronic ground state (e.g. Adler-Golden, 1997). The airglow radiation originates from these and lower levels, which causes dozens of molecular emission bands in the optical and near-IR regime (e.g. Rousselot et al., 2000; Cosby and Slanger, 2007; Noll et al., 2015). Apart from cascades of radiative transitions, the redistribution of the vibrational and rotational level populations is also caused by collisions (Dodd

et al., 1994; Adler-Golden, 1997; von Savigny et al., 2012; Xu et al., 2012; Kalogerakis et al., 2016). In terms of the vibrational relaxation, molecular oxygen ( $O_2$ ) is most important. For the rotational level populations,  $O_2$  and the predominating atmospheric constituent molecular nitrogen ( $N_2$ ) are essential. Collisions involving atomic oxygen mostly lead to a multi-quantum deactivation of the vibrational excitation or even destruction of OH. They are crucial for the observed spread of the emission layer depending on the vibrational level  $v'$  of the upper state of the transition. Higher  $v'$  bands emit at higher altitudes. For  $\Delta v' = 1$ , the differences amount to several hundred metres (von Savigny et al., 2012; Noll et al., 2016).

Apart from the  $v'$ -dependent OH intensity, which is an important tracer of atmospheric chemistry and dynamics, OH emission lines are also very valuable for estimates of the kinetic temperature in the mesopause region. The widely-used approach (e.g. Beig et al., 2003; Schmidt et al., 2013; Reisin et al., 2014) assumes that the population distribution over the lowest rotational levels  $N$  for a fixed  $v$

---

\*Corresponding author

Email address: stefan.noll@uibk.ac.at (Stefan Noll)

equals a Boltzmann distribution that corresponds to the ambient temperature (e.g. Beig et al., 2003; Cosby and Slanger, 2007; Khomich et al., 2008). This requires a sufficient number of thermalising collisions in comparison to the  $v$ -dependent radiative lifetimes between 5 ( $v = 9$ ) and 58 ms ( $v = 1$ ) (Xu et al., 2012). However, a local thermodynamic equilibrium (LTE) is no longer guaranteed in the highest parts of the emission layer, where the  $N_2$  and  $O_2$  densities are low and the counteracting oxygen atoms are numerous. This can lead to non-LTE contributions of several Kelvins to the measured OH rotational temperatures  $T_{\text{rot}}$  (Cosby and Slanger, 2007; Noll et al., 2015, 2016). The exact amount depends on  $v'$  and the line set used. It also varies with time due to changes in the effective height of the emission layer and the corresponding chemical composition. Noll et al. (2016) found that mean nocturnal  $T_{\text{rot}}$  variations for OH bands with high  $v'$  could even be dominated by non-LTE effects.

Investigations of long-term variations of OH intensities (Clemesha et al., 2005; Reid et al., 2014; Gao et al., 2016) and  $T_{\text{rot}}$  (Beig et al., 2003, 2008; Beig, 2011a,b; Huang et al., 2016; Kalicinsky et al., 2016) are particularly interesting since they provide important information on the influence of the solar activity and anthropogenic greenhouse gas emissions on the mesopause region. Such studies require time series which should ideally cover more than a solar activity cycle of 11 years. While remote sensing of OH emission is the approach that is most frequently used to investigate the mesopause region, suitable data sets are still rare. Therefore, any additional time series of sufficient length is very valuable, especially in regions of the world with a lack of data. Moreover, most time series only include a single OH band (e.g. Beig et al., 2003; Schmidt et al., 2013) and well-calibrated OH intensities are not always available. Finally, it is questionable how the solar cycle effects and long-term trends for OH  $T_{\text{rot}}$  are affected by changes in the OH emission layer structure. This is critical since studies of the long-term temperature variations at OH layer heights rely on the suitability of OH  $T_{\text{rot}}$  as a tracer of the kinetic temperature. As discussed before, this might not be fulfilled.

The Very Large Telescope (VLT) of the European Southern Observatory (ESO) at Cerro Paranal in Chile ( $24^{\circ}38' S$ ,  $70^{\circ}24' W$ ) has regularly been operating the Ultraviolet and Visual Echelle Spectrograph (UVES) (Dekker et al., 2000) since April 2000. The archival data of this astronomical instrument allow us to investigate the long-term variations of several OH bands at a high spectral resolution in parallel. Therefore, we have selected a UVES sample of 3,113 high-quality spectra comprising the first 15 years of operation. This data set is the first one covering more than a solar cycle originating from a site located west of the Andes. In South America, longer OH time series were only published for El Leoncito ( $32^{\circ} S$ ,  $69^{\circ} W$ ) in Argentina (Reisin and Scheer, 2002; Scheer and Reisin, 2013) and Cachoeira Paulista ( $23^{\circ} S$ ,  $45^{\circ} W$ ) in Brazil (Clemesha et al., 2005). Apart from a general characterisation of the so-

lar cycle effects and long-term trends in the OH intensity and  $T_{\text{rot}}$ , our study focuses on the contribution of varying non-LTE effects to the  $T_{\text{rot}}$  long-term variations. For this purpose and a comparison of complementary independent data sets, we also investigated OH limb-sounding data and  $CO_2$ -based kinetic temperature profiles from the multi-channel radiometer SABER on the TIMED satellite (Russell et al., 1999). With the start of the archive in January 2002, this data set only has a slightly shorter time coverage than our sample of UVES spectra.

In the following, we will describe the UVES (Section 2.1) and SABER data sets (Section 2.2) for this study in detail. Then, we will address the measurements of OH line intensities and temperatures (Section 3.1), the analysis of the long-term variations for both data sets (Section 3.2), and the estimation of non-LTE effects related to the measured UVES OH  $T_{\text{rot}}$  (Section 3.3). The results for the long-term variations in intensity and temperature, their relation to other observations, and the impact of non-LTE effects on the  $T_{\text{rot}}$  trends will be discussed in Sections 4.1 to 4.3. Finally, we will draw our conclusions (Section 5).

## 2. Data sets

### 2.1. UVES

The high-resolution echelle spectrograph UVES (Dekker et al., 2000) mounted at the VLT covers a maximum wavelength range from 300 to 1100 nm, where up to 500 nm can be observed in parallel by a blue and a red arm, which are fed by means of a dichroic beam splitter. The exact wavelength coverage depends on the selected beam splitter and the order-separating cross disperser. For the investigation of OH emission, we focus on the red arm and set-ups with central wavelengths of 760 and 860 nm covering about 380 nm each. Since the spectra of the red arm are registered by a mosaic of two charge-coupled devices (CCDs), there is a gap of the spectral coverage around the central wavelength, which amounts to about 14 nm. The combined range of both set-ups between about 570 and 1040 nm comprises 15 OH bands with  $v'$  between 3 and 9 (see Noll et al., 2015). The overlapping range of the 760 and 860 nm set-ups covers six OH bands with  $v'$  between 5 and 9. Our study of long-term variations therefore focuses on the OH( $v'-v''$ ) bands (5-1), (6-2), (7-3), (8-3), and (9-4), which neglects the weaker  $v' = 7$  band OH(7-2). OH(4-0) cannot be included since it is located in the central gap of the 760 nm set-up.

The spatial coverage of the sky along the slit axis is  $8''$  for the 760 nm and  $12''$  for the 860 nm set-up. The slit width can be set freely. For a standard width of  $1''$ , the resolving power of the spectrograph is about 42,000. The maximum is 110,000. Therefore, the OH emission lines are usually well separated, as Fig. 1 illustrates for the lower P-branch of the weakest selected OH band (8-3) in a typical UVES spectrum. Even the  $\Lambda$  doublet structure of the OH lines (e.g. Rousselot et al., 2000) is partially resolved. Line

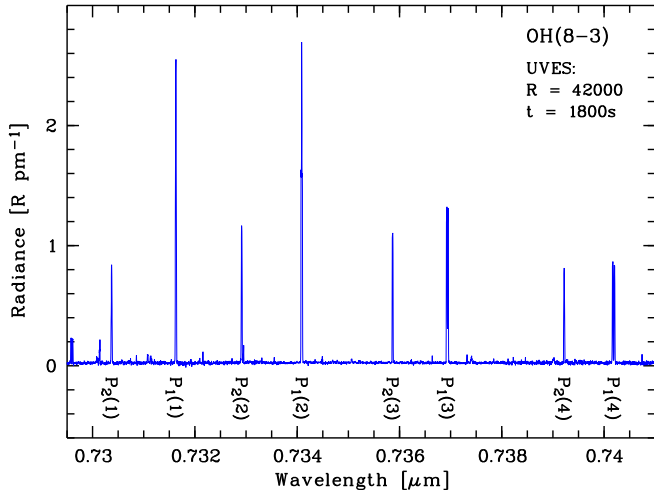


Figure 1: P-branch lines of the OH(8-3) band for a typical UVES sample spectrum with a standard resolving power of 42,000 and nearly average exposure time of 1,800 s. Radiance and wavelength are given in Rayleighs per picometre and micrometres, respectively. Note that the  $\Lambda$  doublets of the higher  $P_1$ -branch lines are partially resolved, which makes these lines broader and flatter.

blends are rare. For a comprehensive overview of UVES airglow spectra, see Hanuschik (2003) and Cosby et al. (2006).

### 2.1.1. UVES data reduction

For this study, we used the UVES-related so-called Phase 3 data products from the ESO Science Archive Facility. These files were produced by means of the ESO data reduction pipeline for UVES and contain wavelength-calibrated one-dimensional spectra with merged echelle orders derived from the initial two-dimensional raw frames. We only considered those data products which include a sky-subtracted spectrum of the astronomical target with and without flux calibration and a spectrum of the sky background derived by the sky subtraction procedure of the pipeline. The latter exhibits the airglow emission during the exposure of the spectrum and is therefore the basis for our analysis.

The sky data from the UVES Phase 3 products are not flux calibrated. First, we corrected these spectra for the variable slit area on the sky in order to be representative of a unit solid angle. Then, we used the object spectra with and without flux calibration to obtain instrument response curves. For this, we also had to consider that the object spectra were corrected for atmospheric extinction using the extinction curve of Tüg (1977). We did not apply this correction to the sky spectra since losses by scattering and absorption differ from those related to point-like continuum sources and are also variable with time. For the investigated wavelength regime, the extinction by atmospheric scattering can be neglected for the extended airglow emission at Cerro Paranal (Noll et al., 2012). The correction of the absorption is described in Sec-

tion 3.1. Depending on instrumental set-up and observing period, different response curves were applied to the UVES Phase 3 products. We identified two response curves for the 760 nm set-up spectra and six for those with a central wavelength of 860 nm. We did not find any significant long-term trend in the curve shape pointing to instrument and telescope efficiency changes. The structure of all curves is very similar independent of the set-up. An exception are wavelength ranges which are affected by strong molecular absorption by  $O_2$  and water vapour (e.g. Noll et al., 2012). This suggests that the response curves are not reliable in these ranges due to an inadequate handling of atmospheric molecular absorption in the spectrophotometric standard star spectra used for flux calibration. Therefore, we scaled the individual response curves to a reference one in a safe wavelength range and then built a master response curve by reliability-dependent weighted averaging and interpolation in the most affected regions. The average shape correction for all covered wavelengths and all spectra is 1.2%. The differences in the flux calibration for lines of the same OH band should be significantly smaller.

For flux-calibrated astronomical spectra, the absolute flux uncertainties are typically of the order of 5 to 10%. This expectation is in agreement with the results of a comparison of the OH band intensities of the UVES data (see Section 3.1) and those of a sample of spectra taken with the VLT echelle spectrograph X-shooter (Vernet et al., 2011) discussed in Noll et al. (2015, 2016) for the overlap period from October 2009 to March 2013. For the investigation of long-term variations in intensity, the relative flux uncertainties have to be distinctly lower. We therefore checked the flux-calibrated spectra from standard star observations which were Phase 3 science targets and compared them with each other and to the corresponding reference fluxes from literature (Hamuy et al., 1994; Moehler et al., 2014). In general, there seems to be a good agreement. However, the response curve correction for the Phase 3 products does not consider flux differences related to the use of observing modes with single and double pixel binning. Taking CCD 1 (with wavelengths shorter than the central gap) of the more popular mode without pixel merging as reference, we found a correction factor of 0.944 for CCD 2 and 1.038 for both chips operated with two-pixel binning. Moreover, 760 nm spectra taken until 2009 show a conspicuous difference in the flux levels related to the two CCDs. Since the Phase 3 products do not contain standard star observations for this set-up, we compared non-standard star spectra that were calibrated with both response curves. As a consequence, we multiplied the fluxes for CCD 2 by a factor, which was 0.875 for two-pixel binning. These corrections reduced the systematic errors significantly. As described in Section 3.2.3, we used the OH line measurements to check the quality of the calibration of the data related to the different observing modes and response curves. The resulting relative flux calibration accuracy is about 2%, which is sufficiently good for studies of long-term variations. Note that this accuracy estimate is mainly based on averages

considering several hundred spectra. For individual observations or rarely applied combinations of observing mode and response curve, the uncertainty is probably higher.

### 2.1.2. UVES sample selection

This study focuses on the first 15 years of UVES data, i.e. spectra taken until March 2015 were considered. For this period, the number of 760 and 860 nm spectra exceeds 10,000. Since the analysis of long-term variations for different OH bands requires a high-quality sample, we reduced the data set by applying several selection criteria. First, we only considered spectra with a minimum exposure time of 5 min to avoid noisy OH lines. This criterion also rejects the spectra with the brightest astronomical targets. The contamination of the sky spectra by emission of astronomical objects is critical since the sky integration procedure of the UVES pipeline only excludes the slit positions which are closer than 25% of the slit length to the target centre. For the 760 and 860 nm set-ups, this limit corresponds to 2 and 3'', respectively. Hence, bright targets, extended objects, or a strong blurring of point-like stellar sources by high atmospheric turbulence can cause a significant contamination of the sky spectrum, which increases the statistical and systematic uncertainties related to the OH line measurements depending on the shape of the object spectrum. For this reason, we applied an additional selection limit based on the average continuum flux at the positions of the measured OH lines. Only spectra with less than  $2,000 \text{ photons s}^{-1} \text{ m}^{-2} \mu\text{m}^{-1} \text{ arcsec}^{-2}$ , i.e. about  $11 \text{ R nm}^{-1}$ , were considered. This limit still allows data taken in moonlit nights to be selected. Furthermore, we rejected spectra observed with very wide slits of more than 2''. This limit corresponds to a minimum resolving power of about 20,000 and avoids possible issues related to the measurement of broad box-shaped lines.

The selection criteria listed so far result in a sample of 3,475 spectra. This data set was then checked for outliers in the derived  $T_{\text{rot}}$  and their uncertainties (Section 3.1). For this, we performed an iterative  $\sigma$ -clipping procedure, where we applied  $5\sigma$  limits for the five OH bands (5-1), (6-2), (7-3), (8-3), and (9-4) relevant for the trend analysis in terms of  $T_{\text{rot}}$ , the  $T_{\text{rot}}$  difference compared to OH(6-2), and the  $T_{\text{rot}}$  uncertainty. The resulting sample optimised for the five bands comprises 1,463 spectra centred on 760 nm and 1,650 spectra centred on 860 nm, i.e. 3,113 spectra in total. Note that the identification of outliers is not a simple task for the investigated sample since the statistical and systematic errors of the individual  $T_{\text{rot}}$  measurements vary due to differences in the exposure time, object contamination, spectral resolution, and line intensity. Therefore, we also performed an alternative selection with the same criteria except for a  $4\sigma$  limit for the  $T_{\text{rot}}$  uncertainty. This slight change reduced the sample to 2,885 spectra, which illustrates that the data distribution cannot be described by a single Gaussian. In order to investigate the effect of the sample selection on the analysis of long-term variations, we performed the entire

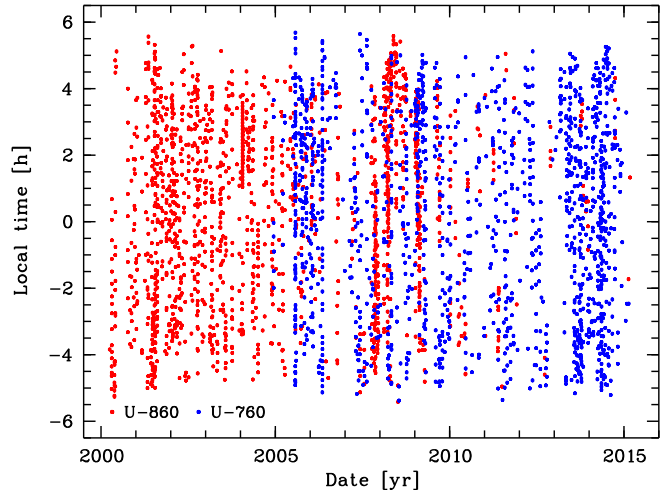


Figure 2: Sample of UVES data used for this study. The local time (i.e. Universal Time corrected for the longitude of Cerro Paranal) of the mid-exposure in hours and the date in years are shown for 1,463 spectra centred on 760 nm (blue) and 1,650 spectra centred on 860 nm (red).

analysis for both samples. The differences were distinctly smaller than the estimated errors, which indicates that our results do not critically depend on the selection criteria. In the following, we will therefore focus on our main sample of 3,113 spectra.

Fig. 2 shows the local solar mean time in hours and the observing date in years for the mid-exposures of our UVES sample spectra. For short time scales, the density of data points is highly variable due to the various possible UVES observing modes, where only a minor fraction fulfils our selection criteria. Moreover, ESO usually operates two to three competitive instruments at the same telescope. For longer periods, the variations are smaller. On an annual basis calculated from April to March, the number of spectra varies between 83 and 385. The standard deviation is about 50% of the mean value. A comparison of the two halves of the covered period shows a difference of less than 5% of the sample size. While the full sample indicates a good coverage of the 15 years, this is not the case for the subsamples of the 760 and 860 nm set-ups. Before 2005, very few 760 nm spectra were taken. Then, ESO started to officially offer this set-up, which became eventually more popular than the 860 nm mode. Since the calibrations of the spectra of both set-ups appear to agree very well (see also Section 3.2.3), this small sample overlap does not seem to be critical for the investigation of the long-term variations. The distribution of local times reflect the fact that astronomical observations are usually carried out at nighttime. The minimum solar zenith angle of our sample is  $102^\circ$ . The few twilight spectra in the full data set were rejected by our continuum flux limit.

Note that we selected additional set-up-specific subsamples, which were used in the course of the investigation

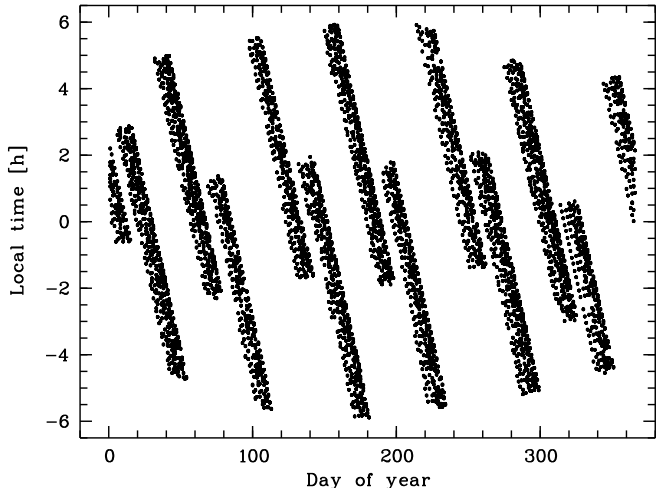


Figure 3: Sample of SABER data used for this study. The local time in hours for the profile data point at 87 km and the day of year are shown for 4,496 profiles. The jumps in local time around midnight for the covered stripes are related to the regular yaw manoeuvres of TIMED (Russell et al., 1999).

of non-LTE effects in Sections 3.3 and 4.3. For these subsamples, the  $\sigma$ -clipping was performed for a higher number of OH bands than we considered for our main sample. We will describe these data sets when they are used.

## 2.2. SABER

The TIMED satellite launched in December 2001 has a slowly-precessing low Earth orbit with an inclination of  $74^\circ$  and a period of 1.6 h and achieves global coverage (except for high latitudes) within 60 days (Russell et al., 1999). SABER performs limb-sounding in ten channels between 1.27 and  $15 \mu\text{m}$  with a vertical resolution of 2 km. For this study, we focus on the two OH-related channels centred on 1.64 and  $2.06 \mu\text{m}$ . Since each channel covers lines of three OH bands, the effective  $v'$  correspond to 4.6 and 8.3 (Noll et al., 2016). Moreover, we consider the  $\text{CO}_2$ -related kinetic temperature  $T_{\text{kin}}$  products. Their elaborate retrieval involves non-LTE radiative transfer calculations (Rezac et al., 2015). For the OH volume emission rate (VER) and  $T_{\text{kin}}$  profiles, we use the version 2.0 products from the SABER data archive for the period from January 2002 (start of the archive) to December 2015. Hence, the SABER time coverage is slighter shorter and shifted to later dates compared to our UVES sample (Section 2.1). Moreover, only nocturnal profiles corresponding to a minimum solar zenith angle of  $100^\circ$  were considered. In order to focus on the VLT region, the profile selection was restricted to the latitude range from  $23$  to  $26^\circ$  S and plus/minus  $10^\circ$  around the longitude of Cerro Paranal of  $70.4^\circ$  W. This selection results in a total number of 4,496 profiles. More details on the selection criteria and the SABER profile characteristics are given by Noll et al. (2016), who performed the same analysis for a SABER data set comprising the years from 2009 to 2013.

Fig. 3 shows the local times and days of year for our SABER sample. The diagram area is only sparsely filled due to the orbital parameters of TIMED. For a specific day of year, one or two narrow time windows are available. The width of the ranges depends on the number of included years. Despite the large gaps, the SABER data are promising for the analysis of long-term variations in comparison to our UVES data set (Fig. 2) since the pattern of coverage is very regular with the mean local time exactly at midnight and a mean day of year of 180. The shift of the annual pattern, which results in  $-12$  to  $-11$  days for the covered period of 14 years, should not be critical.

## 3. Analysis

### 3.1. Measurements of intensities and temperatures

The derivation of UVES OH intensities and  $T_{\text{rot}}$  was carried out in a similar way as described in Noll et al. (2015), where 343 VLT X-shooter spectra with a lower resolving power (3,000 to 18,000) but a wider wavelength coverage ( $0.3$  to  $2.5 \mu\text{m}$ ) were investigated in terms of average nocturnal and seasonal variations.

The line measurements focus on the first four lines ( $N' \leq 4$ ) of the OH  $P_1$  and  $P_2$  branches (see Fig. 1). The transitions of both branches cause an increase of the total angular momentum and involve the OH  $X^2\Pi_{3/2}$  and  $X^2\Pi_{1/2}$  substates, respectively. The considered lines are relatively strong, well separated, and usually used for  $T_{\text{rot}}$  determinations (e.g. Beig et al., 2003; Cosby and Slanger, 2007). It is not possible to measure reliable intensities of all eight lines for each OH band due to contamination by lines of other bands or severe absorption of the emission at lower altitudes of the atmosphere. In principle, the former issue is less critical for UVES than for X-shooter. However, we tried to use the same line selection as described in Noll et al. (2015) for a better comparison and an easier analysis (see also Section 3.3.1). For this reason, we did not consider bands where the UVES spectral coverage was not sufficient to measure all required lines. This criterion resulted in nine OH bands for each of the two set-ups and six bands present in the spectra of both set-ups (see Section 2.1). The OH bands (6-1), (8-2), (9-3) could only be measured in the 760 nm spectra, whereas (3-0), (4-0), and (8-4) were only accessible in the spectra taken with the 860 nm set-up. OH(9-5) was rejected due to the location of the  $P_1(N' = 1)$  line in a gap between two echelle orders, which can happen in the reddest part of the UVES wavelength range. Using the line sets of Noll et al. (2015), the number of considered lines is between 4 and 8. On average, 6.4 P-branch lines were measured.

While strongly absorbed emission lines were excluded from the analysis, lines with a moderate absorption up to several per cent were corrected. As discussed in Noll et al. (2015), the derivation of the effective line-specific absorption requires the calculation of OH line profiles and

high-resolution atmospheric transmission spectra. For the former, Doppler-broadened Gaussian profiles for a typical temperature of 190 K (c.f. Noll et al., 2016) were assumed. The OH line positions originate from the HITRAN2012 database (Rothman et al., 2013). HITRAN is also used as the input for the transmission calculations via the radiative transfer code LBLRTM (Clough et al., 2005), where Cerro Paranal atmospheric mean conditions were assumed (Noll et al., 2012). The resulting line transmissions were corrected for the strongly varying water vapour (see Noll et al., 2015). The column density of this trace gas was derived for each spectrum individually. The continua of the astronomical objects observed in parallel with the airglow emission were sufficiently bright to apply the fitting code `molecfit` (Smette et al., 2015; Kausch et al., 2015). The fit for the water vapour absorption was performed in the wavelength range from 814.0 to 818.3 nm, which is covered by both UVES set-ups. The absorption correction also considers the dependence of the optical depth of the absorber on the zenith angle of the telescope, which varied between 1 and 69° with a mean value of 36°. The formula of Rozenberg (1966) for air was applied for this purpose. The corresponding correction for the OH emission is based on the formula by van Rhijn (1921) for thin layers and a reference altitude of 87 km. For the latter, the mean and maximum horizontal distances of the observed emission from Cerro Paranal are about 70 and 220 km, respectively. Hence, our UVES-based results are related to a geographical area which includes oceanic and mountainous desert regions.

The integration of the line intensities was performed as follows. After the subtraction of the continuum by means of a wide median filter, the line profiles were integrated within spectral intervals with a width of about 3 FWHM and centred on the HITRAN wavelengths. The separation of the  $\Lambda$  doublet was considered for the derivation of the integration limits. In the case of a clear separation of the lines, both components were integrated separately. The final line intensities were then derived by applying the corrections described above to the individual  $\Lambda$  doublet components. For unresolved doublets, the measured intensity was halved for this procedure. For the analysis of the intensity long-term variations, the intensities of all measured lines of an OH band were summed up.

The intensities  $I$  of all measured  $\Lambda$  doublets of an OH band were used to calculate band-specific  $T_{\text{rot}}$ . Assuming a Boltzmann distribution of the population distribution, this can be done by performing a regression analysis for the expression  $\ln(I/(Ag'))$ , including the Einstein  $A$  coefficient and the statistical weight of the upper state  $g'$ , as a function of the energy of the upper state of the transition  $E'$  (Mies, 1974; Noll et al., 2015). The reciprocal of the resulting slope corresponds to  $T_{\text{rot}}$  times a constant. For  $A$ ,  $g'$ , and  $E'$ , we used the OH data in the HITRAN2012 database (Rothman et al., 2013), which are essentially based on the calculations of Goldman et al. (1998). Note that the molecular parameters for OH are still relatively

uncertain (Goldman et al., 1998; Pendleton and Taylor, 2002; Khomich et al., 2008; Brooke et al., 2016). Depending on the data source, the P-branch-related  $T_{\text{rot}}$  results can differ by several Kelvins (Cosby and Slanger, 2007; Noll et al., 2015; Liu et al., 2015; Parihar et al., 2017). Thus, the derived non-LTE contributions to these  $T_{\text{rot}}$  and their change with  $v'$  (see Section 4.3) are also affected. According to Noll et al. (2015, 2016), the HITRAN data provide promising results if only P-branch lines of the same OH band are considered. For this reason and the comparability with the X-shooter-based results, we focused on HITRAN-related molecular data for this study. Moreover, the possible constant temperature offsets are not an issue for the analysis of temporal  $T_{\text{rot}}$  variations. Therefore, the conclusions drawn from this study on long-term variations do not depend on the set of molecular parameters used.

SABER OH VER profile data are available for two channels with effective  $v'$  of 4.6 and 8.3 (Section 2.2). For a comparison with the long-term variations of the UVES-related OH intensities, we performed a vertical integration of the VER profiles for altitude ranges limited by a maximum deviation of 15 km from the mean of both interpolated half-maximum VER heights. For the OH-related temperatures, we used the CO<sub>2</sub>-based kinetic temperature  $T_{\text{kin}}$  profiles and weighted them with the corresponding VERs of the two OH-related channels. We considered the same variable altitude limits as for the VER integration for this calculation in order to avoid systematic errors due to non-zero SABER OH VERs far away from the emission layer (see also Noll et al., 2016). The resulting effective temperatures  $T_{\text{eff}}$  show systematic uncertainties of a few Kelvins (Rezac et al., 2015). Similar to  $T_{\text{eff}}$ , we calculated the effective emission height  $h_{\text{eff}}$  and decadal logarithm of the number density of air molecules  $(\log n)_{\text{eff}}$ , which are used for the discussion of  $T_{\text{rot}}$  non-LTE effects in Section 4.3.

### 3.2. Analysis of long-term variations

Example time series of the intensity and  $T_{\text{rot}}$  measurements discussed in Section 3.1 are shown in Fig. 4 for OH(6-2) and the main sample of 3,113 spectra (Section 2.1.2). For OH(6-2), the full set of eight P-branch lines can be used. This results in a mean integrated intensity of 540 R and a standard deviation of 170 R. The corresponding values for  $T_{\text{rot}}$  are 196.3 and 8.6 K. The mean error related to the regression-based  $T_{\text{rot}}$  derivation for OH(6-2) is 2.5 K, which should be considered as an upper limit for statistical uncertainties because of deviations of the rotational level populations from a Boltzmann distribution due to non-LTE effects (see Section 3.3.1). In any case, the time-dependent variations in Fig. 4 are distinctly stronger than the measurement uncertainties. Moreover, the scatter plots indicate a trend with time for both quantities. The values tend to be higher at the beginning and the end of the time series. This is convincingly confirmed by annual mean values where we considered periods from April

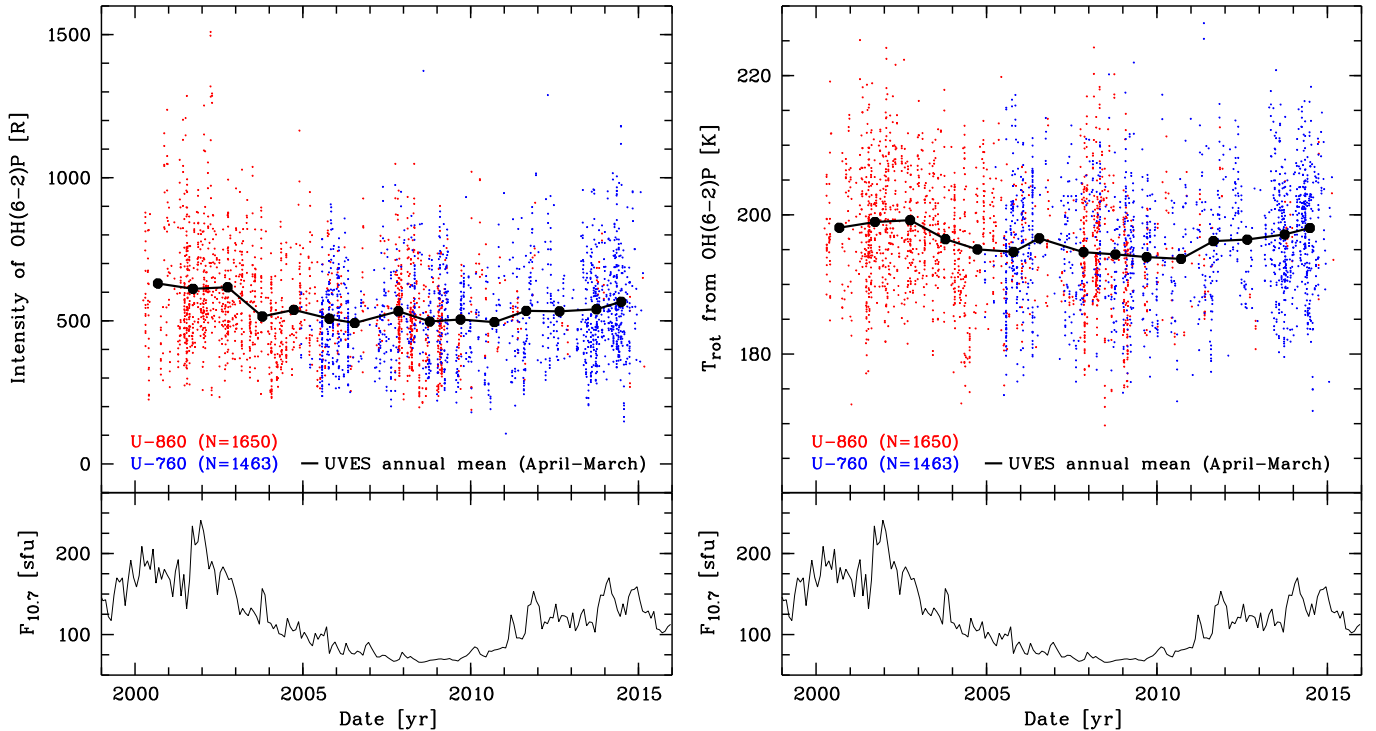


Figure 4: Integrated intensity in R (left) and  $T_{\text{rot}}$  in K (right) for the four lowest  $P_1$  and  $P_2$  branch lines of OH(6-2). The UVES sample is the same as in Fig. 2. Both subfigures also show annual mean values averaged for the period from April to March. Inhomogeneities in the intra-annual data distribution (e.g. in the year 2006) were not corrected. The lower panels display the monthly mean solar radio flux at 10.7 cm in sfu for the period covered by the UVES spectra.

to March in order to avoid incomplete years. For the intensity and  $T_{\text{rot}}$ , the four years with the highest mean values are 2000, 2001, 2002, and 2014. These are also those years with the highest solar activity as measured by the solar radio flux at 10.7 cm (Tapping, 2013), which is a good tracer of the long-term variations of the OH-relevant solar extreme UV (EUV) flux (Dudok de Wit et al., 2008, 2009). It is most frequently used for studies of solar cycle effects in the mesopause region (Beig et al., 2008; Beig, 2011b). The monthly mean values of this  $F_{10.7}$  index are shown in the lower panels of Fig. 4. They are given in solar flux units (sfu), which correspond to 10 kJy. Neglecting a possible long-term trend, a simple linear regression analysis for the annual mean values of the OH(6-2) intensity divided by the 15-year mean and the  $F_{10.7}$  index results in  $19 \pm 2\%$  per 100 sfu. For  $T_{\text{rot}}$ , a similar analysis provides  $4.1 \pm 0.5$  K per 100 sfu. Both results show a significant solar cycle effect for OH(6-2).

In the following subsections, we discuss a more elaborate approach to study the solar cycle effect, the long-term trend, and measurement uncertainties in parallel. Our procedure uses the individual observations instead of annual mean values since these data contain more information on the variation with respect to the solar activity. Moreover, the inhomogeneities in the data samples can better be handled in this way.

### 3.2.1. Correction of data gaps

For the UVES sample, we performed a detrending of the data set in terms of nocturnal and intra-annual variations as a first step in order to avoid possible biases due to data gaps (see Fig. 2). For this purpose, we created a  $12 \times 12$  grid of hours and months. The intensities and  $T_{\text{rot}}$  for the grid points in the bin centres were then calculated by weighted averaging of the values for the individual measurements of the whole sample, which neglects second order effects by year-to-year changes of the nocturnal and seasonal variability pattern. The weights were derived by means of a two-dimensional Gaussian with  $\sigma$  of half an hour and half a month. In this way, data points within a  $1\sigma$  distance from the grid point have similar weight, which is comparable with the result for simple binning and averaging if the data density is high. For sparsely populated cells, the approach makes sure that a sufficient number of values from neighbouring cells contribute to avoid possible issues with low number statistics. Scaling the weight of the centre of the Gaussian to 1, the average weight sum for the relevant nighttime grid points (excluding twilight) was 39 with a standard deviation of 13 for the UVES main sample.

As an example, Fig. 5 shows the grid-based climatologies for the OH(6-2) intensity and  $T_{\text{rot}}$ , which exhibit a dynamical range of the nocturnal variations of about 80% of the mean and 20 K, respectively. These are effects which

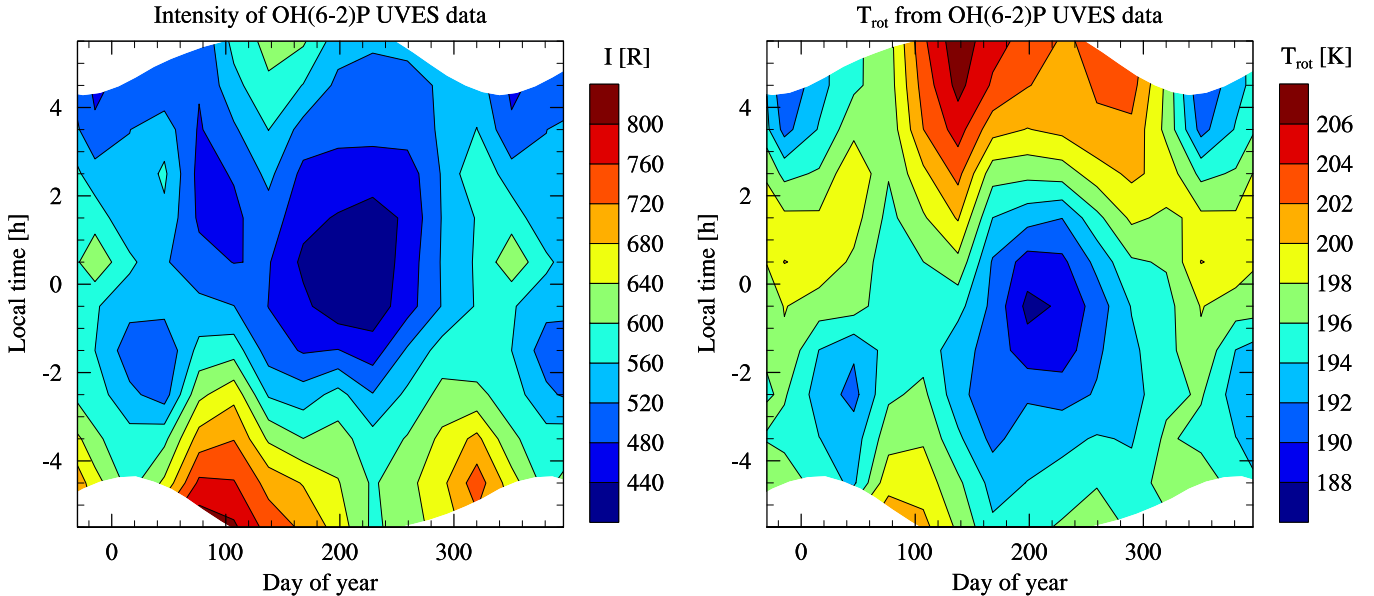


Figure 5: Contour plots of the integrated intensity in R (left) and  $T_{\text{rot}}$  in K (right) of the measured OH(6-2) P-branch lines (see Fig. 4) for a  $12 \times 12$  grid of local times in hours and days of year. The grid points centred on the middle of month and hour were derived by means of smoothing of the 3,113 UVES data points (Fig. 2) via a two-dimensional Gaussian with  $\sigma$  of half a month and half an hour. The contours are only shown for nighttime conditions with solar zenith angles larger than  $100^\circ$ , which are present in the UVES data set.

are distinctly larger than the amplitude of the long-term variations. Therefore, differences in the distribution of the data over the 15-year period for the individual grid points could be neglected for the detrending. Note that the seasonal variability pattern significantly depends on the local time for both quantities, which justifies our two-dimensional detrending approach. While an annual oscillation in intensity and  $T_{\text{rot}}$  with southern hemisphere winter minimum dominates around midnight, a semi-annual oscillation (SAO) tends to be more relevant in the evening and morning. The high impact of the SAO with maxima around the equinoxes and the dependence of the amplitude and phase of the nocturnal variability pattern on season are in good agreement with other OH intensity and  $T_{\text{rot}}$  measurements at similar latitudes as Cerro Paranal (Takahashi et al., 1995, 1998; Gelinat et al., 2008).

The detrending of the UVES data was carried out based on the differences between the closest climatology grid point and the annual nighttime mean. The analysis of the long-term variations with and without detrending for the different OH bands then showed the impact of this correction, which is about  $-0.5\%$  and  $+0.3\text{ K}$  per 100 sfu for the solar cycle effect on average. For the long-term trends, the mean shifts are  $+0.8\%$  and  $-0.1\text{ K}$  per decade. The change in the  $T_{\text{rot}}$  solar cycle effect is the most significant. It is of the same order as the uncertainties of the regression analysis (Sections 3.2.3 and 4.1). The relatively high influence of the removal of the nocturnal and seasonal variations in this case is probably related to the importance of the relatively small fraction of the observations at high  $F_{10.7}$ , which is more affected by inhomogeneities than the

full sample.

We did not perform a similar correction for the SABER sample since the data set is more homogeneous despite the significant gaps (Fig. 3), which suggests that the average nocturnal and seasonal variations have only a small influence if data from different years are compared.

### 3.2.2. Solar cycle proxy

While the parameter for studying the long-term trend is simply the date of observation, the situation is less clear for the solar cycle effect. As already stated, we focus on the solar radio flux index  $F_{10.7}$ . The use of individual observations instead of annual mean values as discussed before requires to average this daily index in an optimal way. The daily measurements are less suitable to trace the solar EUV flux between 10 and 121 nm than averages over a longer period. According to Wintoft (2011), centred averages covering at least half a solar rotational period of 27 days appear to be of similarly good quality. In order to keep the averaged period short, we therefore selected the centred 27-day mean of  $F_{10.7}$  ( $S_{27d}$ ) as our proxy for the solar cycle effect.

In Fig. 6, we show the effect of this decision on the analysis of the UVES OH(6-2) intensity and  $T_{\text{rot}}$  data as given in Fig. 4. For a comparison, the linear regression lines for averages of  $F_{10.7}$  over 1, 27, 81, and 365 days are plotted. As expected, the lines for the daily  $F_{10.7}$  exhibit the largest discrepancy. They are also those with the highest rms (root mean square). The second highest rms are found for the 365-day mean ( $S_{365d}$ ). However, the differences in the slope compared to  $S_{27d}$  are only about  $+0.3\%$



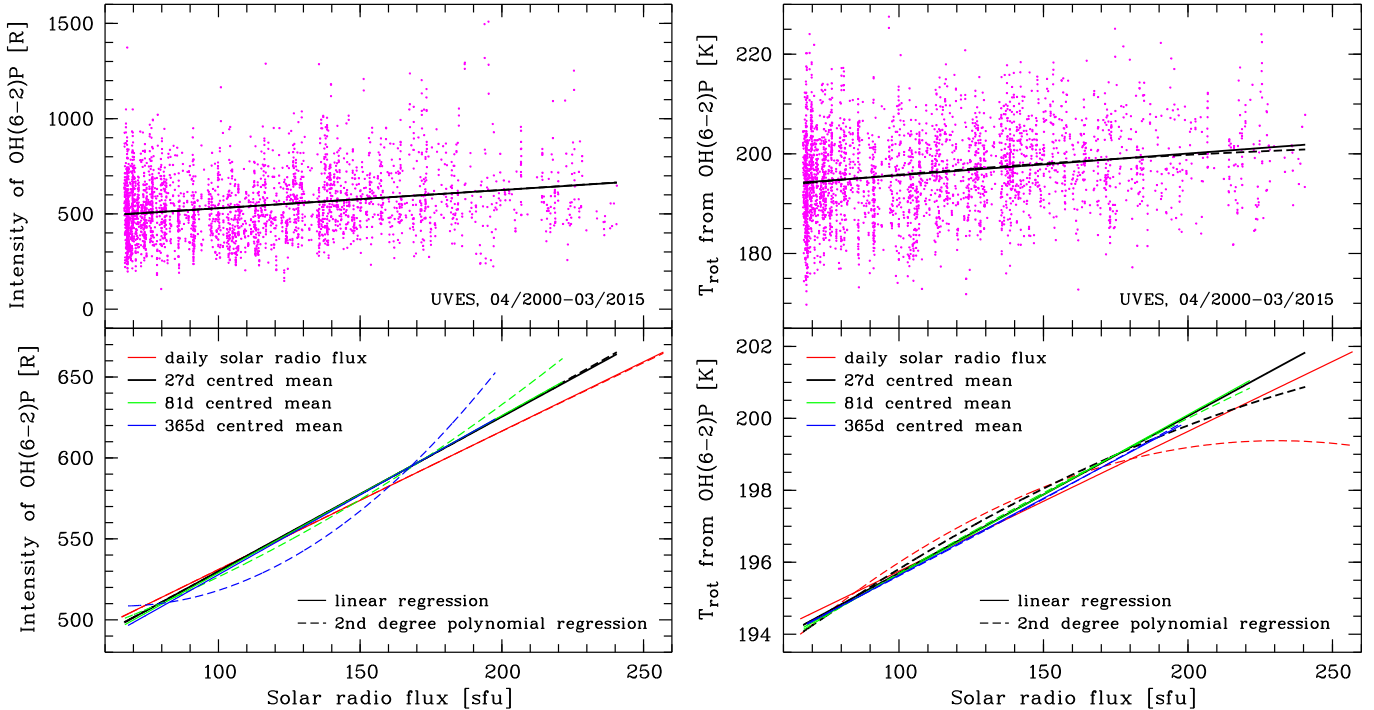


Figure 6: Regression analysis of the relation of the integrated intensity in R (left) and  $T_{\text{rot}}$  in K (right) of the measured OH(6-2) P-branch lines (see Fig. 4) with the solar radio flux in sfu for the full UVES sample (Fig. 2). The individual data points for a centred 27-day mean of the solar radio flux  $F_{10.7}$  ( $S_{27\text{d}}$ ) are plotted in the upper panels, which also show the corresponding regression line (solid) and best second degree polynomial (dashed). The lower panels compare the first and second degree regression results for centred mean  $F_{10.7}$  for 1, 27, 81, and 365 days.

and  $-0.1$  K per 100 sfu. Very small discrepancies are also found for  $S_{81\text{d}}$ . Hence, the choice of  $S_{27\text{d}}$  is sufficient and not critical for the analysis of the solar cycle effect. Fig. 6 also illustrates the reliability of the assumption of a linear relation by showing the results for a second order polynomial regression. In general, these curves are close to those for the linear relations, which supports the linear regression approach. Exceptions are present for  $T_{\text{rot}}$  versus  $S_{1\text{d}}$  and intensity versus  $S_{365\text{d}}$ . The latter might be related to the non-Gaussian distribution of intensities due to a high intensity tail and the relatively narrow range of  $S_{365\text{d}}$  values due to the smoothing of the high solar activity peaks. In this respect, a linear regression is certainly more robust.

### 3.2.3. Regression analysis

Our analysis of the OH intensity and temperature long-term variations in our UVES and SABER samples is based on bilinear regressions involving the parameters observing date and  $S_{27\text{d}}$ . In the case of UVES, we also considered the impact of flux calibration uncertainties on the results.

In order to handle systematic errors related to the UVES  $T_{\text{rot}}$  measurements for the five investigated OH bands, we assumed that there are possible deviations in the response curves for spectra of the 760 and 860 nm set-ups (see Sect. 2.1.2). If this assumption was correct, it would be critical for the analysis, especially for the long-term trend, due to the very different periods covered. The off-

set between the  $T_{\text{rot}}$  of both set-ups was derived for the best overlapping years from 2005 to 2010, when 742 spectra centred on 760 nm and 638 spectra centred on 860 nm were taken. After the correction of the derived  $T_{\text{rot}}$  offsets, the regression analysis was performed for the full sample. The resulting solar cycle effects and long-term trends were then used to detrend the 2005-to-2010 data for another refined derivation of the set-up-related  $T_{\text{rot}}$  differences. Then, the regression analysis was repeated again for the offset-corrected  $T_{\text{rot}}$  of the full sample. The convergence of this iterative procedure was quick due to the low solar activity variations in the comparison period.

The final offsets of the 760 nm  $T_{\text{rot}}$  with respect to the 860 nm ones are between  $-0.7$  and  $+0.4$  K with a sample-related uncertainty of 0.5 K for all bands, i.e. the differences are not significant. Their impact on the results for the solar cycle effect is negligible. The long-term trends for the five OH bands studied increase by about 0.2 K per decade on average. The mean absolute difference of 0.3 K per decade is about half the regression uncertainties. This is also the impact of the uncertainty of the  $T_{\text{rot}}$  correction of 0.5 K. Consequently, the combination of 760 and 860 nm data only causes a minor increase in the uncertainties related to the long-term trends in  $T_{\text{rot}}$ .

The handling of systematic flux calibration errors relevant for the OH intensity analysis is more complex since

eight instrumental response curves (two of them for the 760 nm data) were used for the calibration of the UVES Phase 3 products in different periods. Moreover, there are the UVES operation modes with single and double pixel binning. Finally, the red-arm spectra are registered by two independent CCDs (see Section 2.1). This results in 32 different flux calibration cases containing 7 to 585 spectra of the UVES main sample. We can assume that the deviations are constant factors since wavelength-dependent variations were already corrected (see Section 2.1.1). In order to estimate the flux calibration accuracy and the corresponding uncertainties for the analysis of long-term intensity variations, we performed the bilinear regression analysis for the intensities of the five selected UVES OH bands. Then, we measured the detrended mean intensities for the different combinations of response curve and binning. We especially focused on the bright OH(7-3) band, which is always on CCD 2. For CCD 1, we measured OH(7-2), which originates from the same upper vibrational level  $v' = 7$ . Therefore, it could be detrended with the results for OH(7-3) and the intensity ratio of both bands should be constant, which makes it relatively easy to detect flux calibration errors.

The resulting flux error weighted for the number of spectra in each subsample is 2.0% for CCD 1 and 1.8% for CCD 2, which verifies that our flux calibration corrections discussed in Section 2.1.1 were sufficient. The deviations could even be lower since the statistical uncertainties due to the sample intensity variance also contribute, especially in the case of subsamples with a small number of observations. Moreover, the assumption of a linear model for the solar cycle effect and the long-term trend has some influence (see Section 3.2.2). Next, we used the differences between the mean intensities for each subsample and an (uncritical) arbitrary reference to study their impact on the trend analysis. For this purpose, we subtracted them from and added them to the corresponding individual intensity measurements for each considered band. The differences in the results of a subsequent regression analysis for both modified data sets then indicated the influence of the flux calibration uncertainties on the trend parameters. In general, there is a non-negligible contribution to the final uncertainties in the solar cycle effect and long-term trend related to the intensities of the five investigated OH bands (see Section 4.1). The amount of these systematic effects ranges from 0.35 to 1.76 times the corresponding errors of the regression analysis. The only ratio which is distinctly higher than unity is related to the solar cycle effect for OH(8-3). This could be related to the fact that this band is the only one that is always on CCD 1, which suggests that the results for this chip and the 760 nm set-up appear to be particularly sensitive to flux calibration uncertainties.

### 3.3. Estimation of non-LTE effects

Apart from the characterisation of the long-term variations in UVES and SABER OH data, this study also

focuses on an analysis of the contribution of varying non-LTE effects to the UVES OH  $T_{\text{rot}}$  solar cycle effects and long-term trends.

#### 3.3.1. Correction of systematic temperature errors

In order to quantify the  $v'$ -dependent non-LTE effects, it is required to correct systematic errors in the measured  $T_{\text{rot}}$  of different OH bands. There are instrument-, reduction-, and analysis-related uncertainties. Moreover, the measurements were carried out with band-dependent line sets (see Section 3.1). In this case, the resulting  $T_{\text{rot}}$  differ due to specific non-LTE contributions for each OH line. For the line sets used, this effect can easily amount to several Kelvins (Noll et al., 2015). Based on X-shooter data, Noll et al. (2015) could correct the different systematics by studying 25 OH bands with various possible line sets simultaneously. The UVES data allow us to investigate 12 bands, i.e. nine bands in each set-up. A  $\sigma$ -clipping approach as described in Section 2.1.2 resulted in 1,333 and 1,471 spectra centred on 760 and 860 nm with reliable  $T_{\text{rot}}$  for all measured bands. Studying systematic  $T_{\text{rot}}$  errors only based on the 12 OH bands in the UVES data would probably lead to less accurate results than the X-shooter-related analysis. Therefore, we combined the UVES and X-shooter data to obtain improved reference  $T_{\text{rot}}$  for each  $v'$ .

A joint analysis of both data sets requires the correction of  $T_{\text{rot}}$  differences by discrepancies in the time coverage. The 343 X-shooter spectra were taken between October 2009 and March 2013, which is much shorter than the 15 years of UVES. Therefore, we took the results of our analysis of long-term variations (Sections 3.2 and 4.1) to correct the solar cycle effects and long-term trends in the X-shooter and two UVES data sets. Since the  $v'$  of the bands to be corrected range from 2 to 9 but the trend parameters only cover the range from 5 to 9, we used  $v'$ -independent average coefficients. The reference  $S_{27\text{d}}$  index and date for the results are 100 sfu and New Year of 2011. The nocturnal and seasonal variations can be corrected as described in Section 3.2.1. Since the variability pattern significantly depends on  $v'$  (see Noll et al., 2015), we prepared a sample of 1,526 spectra of the 860 nm set-up optimised for the OH bands (3-0), (4-0), (5-1), (6-2), (7-3), (8-3), and (9-4). Assuming that the nocturnal and seasonal variations are similar for the different samples, we directly corrected the OH bands with  $v'$  between 3 and 9. For the OH(2-0) band, which is only present in the X-shooter data, we applied the OH(3-0)-related climatology. For the correction of the differences in the band-specific line sets, we used the  $T_{\text{rot}}$  shifts derived by Noll et al. (2015), which are between  $-10.4$  and  $-3.4$  K for the OH bands covered by the UVES data. Moreover, we changed the reference line set from the first three  $P_1$ - and  $P_2$ -branch lines to  $P_1(N' = 1)$ ,  $P_1(2)$ , and  $P_1(3)$  only. According to Noll et al. (2016), this is related to a general  $T_{\text{rot}}$  increase of 3.0 K. Afterwards, we derived the sample- and band-related mean  $T_{\text{rot}}$ .

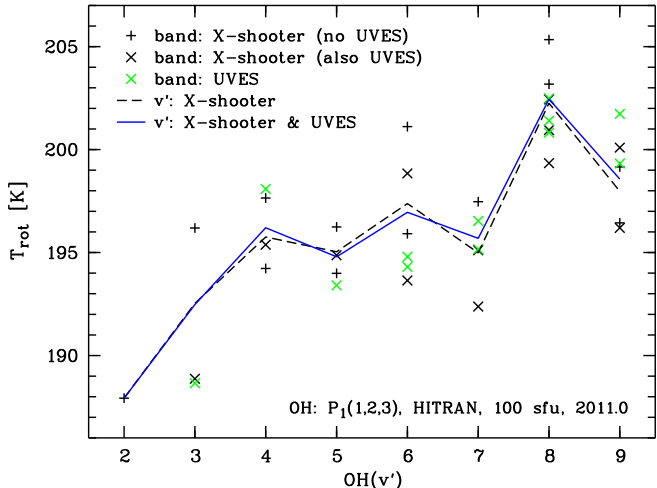


Figure 7: Mean  $T_{\text{rot}}$  in K for 25 OH bands based on the UVES data set of this study (green  $\times$  symbols) and the X-shooter data set of Noll et al. (2015) (black  $\times$  and  $+$  symbols, the latter indicating bands without UVES data). All mean values refer to the first three  $P_1$ -branch lines, HITRAN molecular parameters, a reference solar radio flux of 100 sfu, and the start of year 2011. The plot also shows average  $T_{\text{rot}}$  for fixed  $v'$ . While the dashed curve connects mean values only considering X-shooter data, the solid curve is related to mixed UVES and X-shooter results, where first the band-specific and then the  $v'$ -related averages were calculated.

Fig. 7 shows the results of these calculations.  $T_{\text{rot}}$  for the 25 X-shooter- and 12 UVES-related OH bands are indicated. For the six bands which are present in the spectra of both UVES set-ups, we give the arithmetic mean of the two measurements. In the next step, we averaged the band-specific  $T_{\text{rot}}$  for both instruments, which indicate a mean absolute difference of 1.9 K. Finally, we derived the mean values of all bands with the same  $v'$ . The scatter of the band-specific  $T_{\text{rot}}$  is only 2.2 K. The resulting  $T_{\text{rot}}(v')$  function reveals a trend of increasing  $T_{\text{rot}}$  with increasing  $v'$  and higher temperatures for even  $v'$  compared to the results for adjacent odd  $v'$ . A clear maximum is found for  $v' = 8$ . This remarkable pattern was first identified by Cosby and Slanger (2007) and further studied by Noll et al. (2015, 2016) based on the discussed X-shooter data. It can only be explained by considering non-LTE effects. Adding the UVES data to the X-shooter data does not significantly change the structure of the function. The deviation is less than 1 K for each  $v'$ . We can use the final  $T_{\text{rot}}(v')$  function to correct the systematic uncertainties in the band-specific  $T_{\text{rot}}$ . This works quite well at least for  $v' \geq 4$ , where data of several bands can be combined. The resulting absolute corrections for the 12 UVES OH bands were 1.7 K on average.

### 3.3.2. Linking UVES with SABER temperature data

Noll et al. (2016) showed that the non-LTE effects vary with time and the variations are weaker for OH bands with lower  $v'$ . Therefore, the comparison of  $T_{\text{rot}}$  for very different  $v'$  can be used to study the variability of the non-

LTE contributions. For this purpose, it is necessary to eliminate the differences due to the  $v'$ -dependent VER-related weighting of the altitude-dependent kinetic temperatures  $T_{\text{kin}}$ . This can be achieved by using the SABER OH VER and  $T_{\text{kin}}$  profiles (Section 2.2). Following Noll et al. (2016), we calculated  $v'$ -dependent normalised OH VER profiles based on the two SABER channels with effective  $v'$  of 4.6 and 8.3 by assuming a positive linear relation between emission height and  $v'$  (see von Savigny et al., 2012) and by averaging the profile shapes of both OH VER profiles. For our SABER sample, the mean difference in the VER-weighted effective emission height  $h_{\text{eff}}$  is 0.39 km for  $\Delta v' = 1$ . The scatter amounts to 0.15 km. Next, we derived VER-weighted effective temperatures  $T_{\text{eff}}$  for each  $v'$  by combining OH emission and  $T_{\text{kin}}$  profiles. The resulting mean  $T_{\text{eff}}$  difference for  $\Delta v' = 1$  based on the  $T_{\text{eff}}$  for  $v' = 2$  and 9 is only 0.01 K, i.e. there is no significant temperature gradient for the OH emission altitudes on average. Although the scatter of 0.56 K is distinctly higher, this means that for long-term averages the effect of the  $T_{\text{kin}}$  gradient on the OH  $T_{\text{rot}}$  measurements seems to be relatively small. Consequently, the structures in Fig. 7 should be dominated by non-LTE effects.

The difference of the  $T_{\text{eff}}$  for two given  $v'$  can be used to remove the effect of the ambient temperature profile on the difference of the  $T_{\text{rot}}$  for OH bands with the same two  $v'$ . For this, the individual UVES observations have to be combined with suitable SABER profiles. Since an exact match is not possible, each UVES  $T_{\text{rot}}$  was linked to SABER  $T_{\text{eff}}$  data at similar observing times and days of year. Following Noll et al. (2016), this was done as described for the climatology grid in Section 3.2.1 but with the times and dates of the individual UVES observations as reference instead of a regular grid. Unlike Noll et al. (2016), where only 3.5 years of data were studied, we also considered the solar cycle effect. For this, the results of a linear regression of the SABER  $T_{\text{eff}}$  data and  $S_{27\text{d}}$  were used. The solar cycle correction was calculated by deriving the  $S_{27\text{d}}$  difference between a UVES observation and the corresponding SABER-weighted mean and applying the regression slope. Apart from  $T_{\text{eff}}$ , the SABER-based parameters  $h_{\text{eff}}$  and  $(\log n)_{\text{eff}}$  (see Section 3.1) were processed in the same way to link UVES and SABER data. It is clear that the agreement between the considered quantities of both data sets cannot be particularly good if single UVES observations are studied. The weighted averaging of the SABER data cancels out aperiodic variations. For the weight sum defined in Section 3.2.1, we obtain a mean of 60 and a scatter of 27. Therefore, the described procedure is only reliable for studies of large samples. This criterion is fulfilled for the discussion in Section 4.3.

## 4. Results and discussion

### 4.1. Long-term variations

We investigated the solar cycle effect and long-term trend in intensity and  $T_{\text{rot}}$  for five OH bands with  $v' = 5$

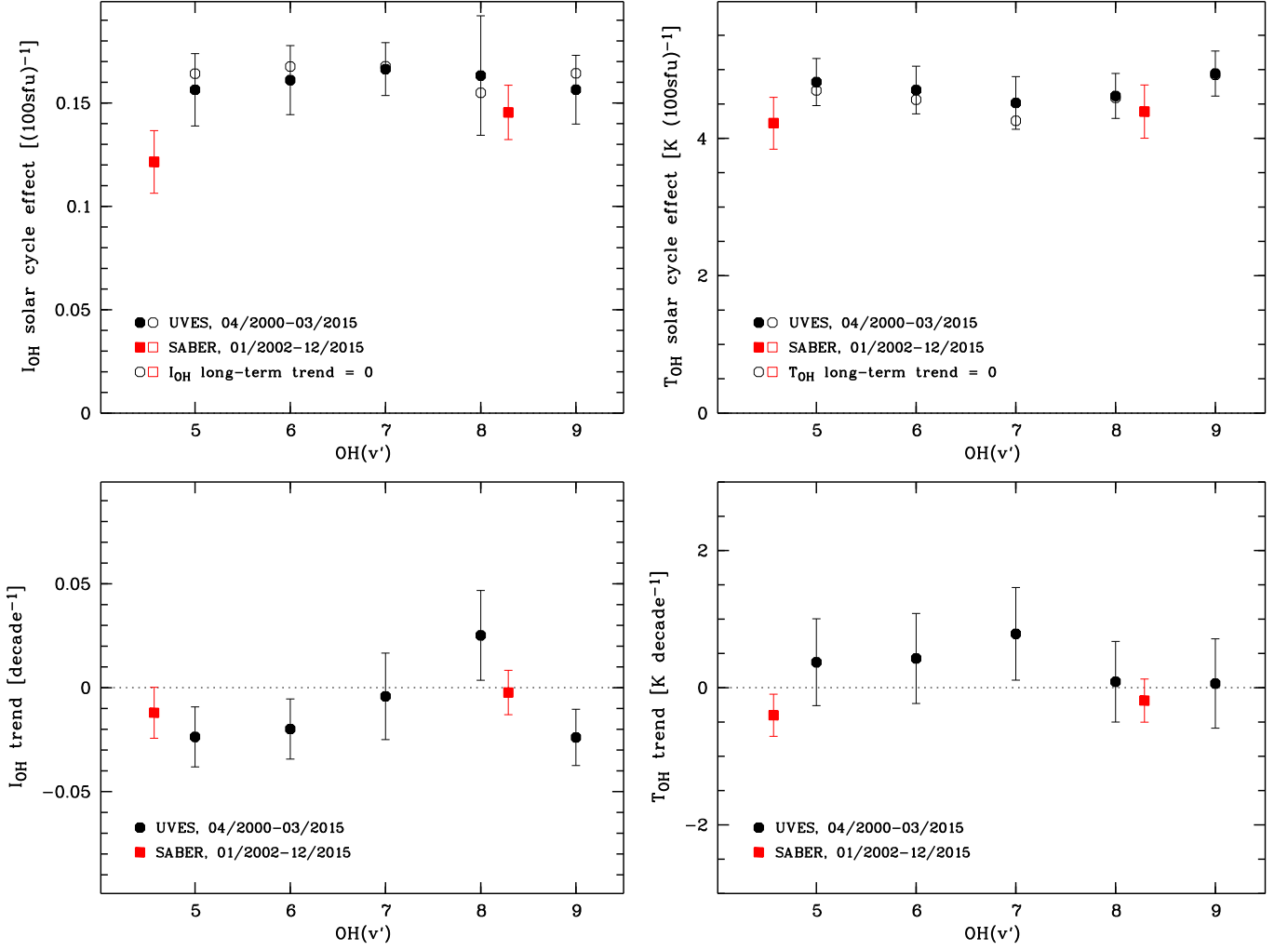


Figure 8: Solar cycle effects per 100sfu (top panels) and long-term trends per decade (bottom) for the relative OH intensity (left) and  $T_{\text{rot}}$  in K (right) for five OH bands measured in the UVES data (circles) and both SABER OH channels (squares). The filled symbols are related to a linear regression analysis involving the solar radio flux  $S_{27\text{d}}$  and the observing date. For the open symbols, possible long-term trends were neglected. The error bars (only shown for the filled symbols) consider regression and for the UVES data also flux calibration uncertainties. Note that averaging of results for different OH bands does not significantly decrease the errors. However, the uncertainties are lower if results of different OH bands are compared.

to 9 measured with UVES at Cerro Paranal. The results for our sample of 3,113 spectra taken between April 2000 and March 2015 are based on a bilinear regression analysis, which was also carried out for a sample of 4,496 SABER OH VER profiles representative of  $v' \approx 4.6$  and 8.3. The selection includes nocturnal profiles taken close to the Cerro Paranal region and within the period from January 2002 to December 2015. The investigated SABER-related quantities were column-integrated VER and  $T_{\text{eff}}$ . The resulting slopes of the regression analysis for both samples are shown in Fig. 8.

The OH band intensities relative to the UVES sample mean indicate solar cycle effects between +15.6 and +16.6% per 100sfu for the individual bands. The uncertainties of these percentages are about 1.6% per 100sfu, except for OH(8-3), where 2.9% per 100sfu is found. The

latter value is dominated by flux calibration errors, whereas the other uncertainties are mainly related to the bilinear regression (see Section 3.2.3). Although the real uncertainties could even be higher due to possible additional systematics, there appears to be a highly significant solar cycle effect. The results for the five OH bands do not show any clear trend with  $v'$ . This statement remains valid if it is taken into account that the uncertainties for comparisons of intensities for different OH bands are smaller than those for the total effect. Consequently, we can average the effects for the different bands, which results in  $+16.1 \pm 1.9\%$  per 100sfu. The solar cycle effects of  $+12.1 \pm 1.5$  and  $+14.5 \pm 1.3\%$  per 100sfu for the two SABER OH channels agree quite well with the UVES-related findings in terms of the total amount of the effect and the absence of a significant  $v'$ -dependent trend. The deviations from the

higher UVES-related values are less than  $2\sigma$ .

The UVES data do not show a significant long-term trend. The mean effect is about  $-1 \pm 2\%$  per decade and the significance for the individual measurements is below  $2\sigma$ . The long-term trend in the OH intensity is the most uncertain parameter of our analysis. It is very sensitive to data calibration issues, as the offset in the trend for OH(8-3) indicates. Nevertheless, the SABER-related results fully agree. The trends for both OH channels are consistent with zero, although the errors are distinctly smaller than those for the UVES data. As illustrated by Fig. 8, neglecting a long-term trend does not significantly change the results for the solar cycle effect. The mean absolute difference for the UVES-related trends would only be  $0.6\%$  per 100sfu. For SABER, no effect is visible.

The results for the temperature are very similar. There is no significant long-term trend. The mean values for  $T_{\text{rot}}$  and  $T_{\text{eff}}$  are  $+0.3 \pm 0.7$  and  $-0.3 \pm 0.3$  K per decade. The solar cycle effect in  $T_{\text{rot}}$  is the most robust trend parameter that we could determine for the UVES data set. The effects for the individual OH bands vary between  $+4.5$  and  $+4.9$  K per 100sfu with a mean value of  $+4.7 \pm 0.4$  K per 100sfu. We do not find a dependence of the solar cycle effect on  $v'$ . The SABER-related data sets for  $v' \approx 4.6$  and  $8.3$  show  $+4.2 \pm 0.4$  and  $+4.4 \pm 0.4$  K per 100sfu. These values are lower than the UVES-related mean effect but with a significance of less than  $1\sigma$ .

In conclusion, 15 years of UVES and 14 years of SABER data show a significant positive solar cycle effect but no discernible long-term trend in OH intensity and temperature for the Cerro Paranal region. Based on the more precise SABER results for the long-term trend, effects beyond the intervals from  $-5$  to  $+3\%$  and  $-1.4$  to  $+0.8$  K per decade can be excluded with  $3\sigma$  confidence. The derived numbers certainly depend on the covered period. An interval of 14 to 15 years is relatively short for studying long-term trends. It is possible that the trends cannot fully be separated from solar cycle effects. In our case, the very high solar activity at the beginning of the time series, especially for UVES, is an issue since  $F_{10.7}$  values typical of the maximum of solar cycle 23 are not found in cycle 24 (see Fig. 4). As illustrated by Fig. 8, the solar cycle effects of about  $15\%$  and  $4$  to  $5$  K per 100sfu are almost unaffected by the uncertainty in the long-term trends.

Our results for the solar influence can depend on the range of  $F_{10.7}$  values covered by the sample. In order to investigate this effect, we split the UVES sample between March and April 2008 as well as the SABER sample between December 2007 and January 2008 to separate the two solar cycles covered and to keep periods of whole years. Then, we measured the solar cycle effects (neglecting long-term trends) in intensity and temperature for the two subsamples. Here, we focus on the results for the UVES OH(6-2) band and the  $v' \approx 4.6$  SABER channel since we do not see a significant  $v'$  dependence. There are remarkable differences in the slopes. The solar cycle temperature effects in the UVES and SABER data for cycle 24

are about  $101 \pm 27$  and  $50 \pm 28\%$  stronger than for cycle 23. The slope for the UVES data taken in cycle 24 indicates a very large value of  $+7.2 \pm 0.6$  K per 100sfu. In the case of the intensity, the cycle 24 data of both instruments show effects which are about  $20\%$  stronger, but these differences are not significant. The temperature-related results could be explained by the weak possible flattening of the  $T_{\text{rot}}-S_{27\text{d}}$  relation for high  $S_{27\text{d}}$  indicated in Fig. 6. However, note that the mean  $S_{27\text{d}}$  indices for both UVES subsamples are still similar with 122 and 102 sfu. As an additional check, we calculated the solar cycle effects in cycle 23 for  $S_{27\text{d}} \leq 166$  sfu, which corresponds to the highest value found in our cycle 24 samples. The percentages for the change of the solar impact in cycle 24 relative to cycle 23 are then  $28 \pm 20$  and  $56 \pm 40\%$ . The effect for the UVES sample decreased a lot but the SABER-related difference is even slightly higher. Therefore, non-linearities in the  $T_{\text{rot}}-S_{27\text{d}}$  relation could be an explanation. It is also possible that the solar cycles 23 and 24 could be different in terms of the response of the mesopause temperature to solar forcing. In any case, these results show that the derived solar cycle effect appears to depend on the covered period.

## 4.2. Comparison to literature

### 4.2.1. Temperatures

The UVES-related mean solar cycle effect for  $T_{\text{rot}}$  from five OH bands is  $+4.7 \pm 0.4$  K per 100sfu. This value can be compared with results from independent measurements to better understand the impact of geographical location, covered period, and measurement approach. For SABER archival data, we have already done this. The mean for the two OH-related channels is  $+4.3 \pm 0.4$  K per 100sfu, which is only slightly lower. This is in good agreement despite possible remaining systematic effects due to differences in the period (see Section 4.1), observational gaps, the relatively large area where the SABER profiles originate from, and that  $T_{\text{rot}}$  are compared with non-LTE-corrected  $T_{\text{kin}}$  (for the latter see Section 4.3).

The impact of the geographical location on our results can be estimated by comparing our SABER-related trends with those of other more global investigations of SABER data. Huang et al. (2016) studied zonal average  $T_{\text{kin}}$  profiles for the years from 2002 to 2014. For  $25^\circ$  S, i.e. the latitude of Cerro Paranal, their altitude-latitude map for the solar cycle effect shows values increasing from about  $2.5$  to  $4$  K per 100sfu for OH-relevant heights from  $80$  to  $100$  km. Hence, our SABER-related response appears to be somewhat stronger. Nath and Sridharan (2014) investigated the average effect in the latitude range from  $10$  to  $15^\circ$  N for the period from 2002 to 2012. Their regression analysis resulted in a slope of  $4$  to  $5$  K per 100sfu for OH emission altitudes, which is in better agreement with our values. The slope could even be higher by a few tenths of a Kelvin for Cerro Paranal if the latitude-dependent results of Huang et al. (2016) are used for an extrapolation of the Nath and Sridharan (2014) values. According to Huang et al. (2016), the discrepancies between both

SABER-based publications can be explained by differences in the regression model used. In contrast to Huang et al. (2016), Nath and Sridharan (2014) did not include seasonal and nocturnal variations. Since this is also the case for our analysis of SABER data, this could explain the better agreement.

There are further reasons for discrepancies between our and the published data. We only considered nocturnal SABER measurements with solar zenith angles above  $100^\circ$ . This limitation can cause systematic deviations if there is a significant dependence of the  $T_{\text{kin}}$  long-term variations on local time. We did not include quasi-biennial oscillations in our analysis. However, these variations should be sufficiently independent of the long-term variations. Finally, both publications cover a shorter period than our SABER sample and do not consider longitudinal variations, which could be as high as latitudinal variations. Therefore, it is difficult to explain the differences in detail.

The SABER-related studies also contain information on the long-term trend. Nath and Sridharan (2014) included this effect in their regression model and found trends between  $-1$  and  $0$  K per decade for the OH emission heights, with smaller absolute values at higher altitudes. Huang et al. (2016) neglected a long-term trend for their final analysis since they did not find a significant impact on their results for the solar cycle effect, which is in good agreement with our findings.

For a direct evaluation of our UVES-based results, other ground-based OH measurements are best suited. In terms of latitude, the OH(6-2) observations at Cachoeira Paulista ( $23^\circ$  S) are the closest. For the years from 1987 to 2000, Clemesha et al. (2005) found a  $T_{\text{rot}}$  11-year oscillation with an amplitude of  $+6.0 \pm 1.3$  K, which corresponds to about 9 K per 100 sfu (Beig et al., 2008). Their long-term trend is highly negative with  $-10.8 \pm 1.5$  K per decade. However, the difference in  $T_{\text{rot}}$  for years of maximum and minimum solar activity is only about 5 K for their data set, which well agrees with our observations (see Fig. 4). Therefore, it appears that solar cycle effect and long-term trend influence each other in the analysis of Clemesha et al. (2005). Values consistent with our results could have been possible as well. Nevertheless, an exact match is not expected because of the very different period studied. A more negative long-term trend for their study would even be consistent with the observations of a weakening of the cooling trend over several decades (Beig, 2011a).

Another station with a long OH(6-2)  $T_{\text{rot}}$  time series in South America is El Leoncito ( $32^\circ$  S). Considering only the years from 1998 to 2002, Scheer et al. (2005) found  $+0.9 \pm 0.3$  K per 100 sfu for a fitted trend of  $-2.7$  K per decade. Without a trend, the result was  $-0.1 \pm 0.3$  K per 100 sfu, i.e. a solar cycle effect was not significant. This divergent finding could be related to the different and also very short period covered. As discussed in Section 4.1, this can be critical. Scheer and Reisin (2013) also considered data taken between 2006 and 2011. Under the assumption of no

solar cycle effect, they derived a long-term trend of  $-2.1 \pm 0.6$  K per decade. As in the case of Clemesha et al. (2005), their data can also be interpreted in a different way. Their annual mean  $T_{\text{rot}}$  for years of high and low solar activity differ by about 3 K. This is smaller than the 5 K that we obtain for the same years in the UVES sample (Fig. 4). If we assume that the long-term trend is close to zero, as the UVES and SABER data indicate, this would suggest a solar cycle effect of 2 to 3 K per 100 sfu at El Leoncito. The difference in the response to solar forcing compared to Cerro Paranal might be related to the observing site. The latitude difference is  $7^\circ$  and El Leoncito is located on the other side of the Andes.

For further comparisons to OH-related data sets with a good time coverage, we have to consider data from northern mid-latitudes. The corresponding results have to be taken with care since the analysis of SABER data by Huang et al. (2016) suggests that the solar cycle effect at their limiting latitude of  $48^\circ$  N could be stronger by about 1 K per 100 sfu than at  $25^\circ$  S. A very long continuous ground-based time series of OH(3-1) data starting in 1988 is from Wuppertal ( $51^\circ$  N) in Germany. Kalicinsky et al. (2016) derived  $4.2 \pm 0.9$  K per 100 sfu and  $-0.9 \pm 0.6$  K per decade for these data and a linear regression approach. However, they noticed that a linear long-term trend does not fit the data well. A better model appears to be an oscillation with a period of  $25 \pm 3$  years and an amplitude of  $2.0 \pm 0.4$  K. It results in a response to solar activity of  $4.1 \pm 0.8$  K per 100 sfu, which is in good agreement with our findings. Their solar cycle effect appears to be relatively stable over the three activity maxima covered, which does not support the possible difference for cycle 23 and 24 found in our data (see Section 4.1). If the oscillation model was realistic, it would cause a negative long-term trend for the period covered by our data. There could also be site-related effects, which could explain why we do not see such a trend. In general, the published studies related to different measurement approaches and mid-latitude observing sites reveal long-term trends which are slightly negative or consistent with zero (Beig, 2011a). The corresponding solar cycle effects are of the order of several Kelvins (Beig, 2011b). As another example, Pertsev and Perminov (2008) derived an effect of about 4.5 K per 100 sfu based on OH(6-2) measurements at Zvenigorod ( $56^\circ$  N) near Moscow in Russia for the years 2000 to 2006.

All these results suggest that the spatial and temporal differences in the solar cycle effects and long-term trends for temperatures at OH emission heights for low to mid-latitudes are only moderate and that our Cerro Paranal results are in good agreement with them.

#### 4.2.2. OH intensities

Our UVES data for five OH bands show a mean relative solar cycle effect of  $+16.1 \pm 1.9\%$  per 100 sfu. This is only slightly higher than our result for the two SABER OH channels, which is  $+13.3 \pm 1.9\%$  per 100 sfu on average. Gao et al. (2016) studied the response of solar radiation

to OH intensities also based on SABER data. For the period from 2002 to 2014, local times within a radius of 3 h around midnight, and latitudes up to  $50^\circ$  in both hemispheres, they found  $11.4 \pm 1.3$  and  $12.9 \pm 1.1$  % per 100 sfu for the two channels centred on 1.64 and 2.06  $\mu\text{m}$ . These global averages only deviate by a few tenths per cent from the values for a latitude of  $25^\circ$  S. Although the latitude of Cerro Paranal is close to a minimum for the southern hemisphere, this similarity in the results is possible due to systematically lower effects in the northern hemisphere. The solar cycle sensitivity derived by Gao et al. (2016) is only about 1% per 100 sfu lower than the outcome of our regression analysis. This deviation is not significant. The measurement of peak emission rates, the differences in the local time coverage, zonal averages, and the use of annual mean values by Gao et al. (2016) could contribute to the small difference. The regression analysis was performed with and without linear long-term trend. However, the results for the solar cycle effect were almost identical, which is consistent with our findings.

Ground-based studies of OH intensities are less frequent than those of OH  $T_{\text{rot}}$ . In most cases, both quantities were discussed together (c.f. Section 4.2.1). For Cachoeira Paulista and OH(6-2), Clemesha et al. (2005) found an amplitude for the 11-year oscillation of  $14 \pm 4$  %, which corresponds to about  $+21 \pm 6$  % per 100 sfu if we assume the same conversion as Beig et al. (2008) used for  $T_{\text{rot}}$ . The effect tends to be higher than for Cerro Paranal but the difference is not significant. The corresponding long-term trend is  $+2.2 \pm 0.5$  % per decade. The amount is within the range of our OH measurements. However, with the relatively small uncertainties given, there would be a weak positive trend for the years from 1987 to 2000. Scheer et al. (2005) studied the long-term OH(6-2) intensity variations at El Leoncito. Since their data set only covers the years from 1998 to 2002, we focus on their result for a regression analysis without long-term trend, which is  $-1.8 \pm 1.5$  % per 100 sfu. This lack of a significant solar cycle effect is similar to the situation for  $T_{\text{rot}}$  described in Section 4.2.1. It also appears to be an apparent effect due to the limitations in the data set without periods of low solar activity. In order to prove this assumption, it would be necessary to perform a detailed analysis of the mostly unpublished OH(6-2) intensity data taken since 2006 (c.f. Scheer and Reisin, 2013), which cover periods of high and low solar activity. Reid et al. (2014) studied OH(8-3) intensity data taken between 1995 and 2010 at Buckland Park ( $35^\circ$  S) near Adelaide in Australia. Their multiple harmonic analysis resulted in an amplitude of  $6 \pm 5$  % for the solar 11.2-year period, which suggests a linear solar cycle effect of less than 10% per 100 sfu. However, the very large uncertainty does not allow us to detect a significant difference in comparison to our and the other measurements.

For the northern mid-latitude station Zvenigorod, Pertsev and Perminov (2008) report a solar cycle sensitivity of  $+30 \pm 4$  % per 100 sfu within the period from 2000 to 2006. This large effect was obtained by means of OH(6-2) but it

would be similar for other OH bands which were measured in their spectroscopic data. The lack of a  $v'$  dependence is consistent with our UVES-based results. The large discrepancy between the solar cycle effects for Zvenigorod and Cerro Paranal could be explained by the large latitude difference. The SABER-based analysis by Gao et al. (2016) shows a maximum-to-minimum ratio of 2 for the latitude range from  $50^\circ$  S to  $50^\circ$  N. Zvenigorod at  $56^\circ$  N is outside this range. However, the steep increase of the solar cycle effect towards higher latitudes could be sufficient to significantly reduce the discrepancy between the Pertsev and Perminov (2008) and our results.

Our discussion of the few studies on the OH intensity long-term variations in the last two solar cycles shows that our knowledge is still poor. Therefore, our combined study of UVES and SABER data provides important constraints especially on the OH intensity solar cycle effect at low latitudes.

#### 4.3. Non-LTE contributions to OH rotational temperatures

The difference of 0.4 K per 100 sfu between the mean solar cycle effects for the UVES OH  $T_{\text{rot}}$  and SABER OH  $T_{\text{eff}}$  (see Section 4.1) could significantly be affected by long-term variations in the non-LTE contributions to OH  $T_{\text{rot}}$ ,  $\Delta T_{\text{NLTE}}$ . On nocturnal and seasonal time scales, the variability of these effects can be very crucial for interpreting the total  $T_{\text{rot}}$  variations, as shown by Noll et al. (2016). It seems that these variations are correlated with changes in the height and shape of the OH emission layer since this affects the ratio of OH production, thermalisation by  $\text{N}_2$  and  $\text{O}_2$  collisions, and OH deactivation and destruction by atomic oxygen. Our sample of UVES data allowed us to study this relation in detail.

##### 4.3.1. Relation to effective emission height and density

Noll et al. (2016) showed that the quantification of the varying non-LTE effects works best if the  $T_{\text{rot}}$  of an OH band with low  $v'$  is used as reference since the corresponding variations appear to be distinctly weaker than those for bands with higher  $v'$ . Noll et al. (2016) could use OH(2-0) for this purpose. The band with the lowest  $v'$  in the UVES wavelength range is OH(3-0). The X-shooter-based study of the nocturnal  $\Delta T_{\text{NLTE}}$  variations indicated that the changes related to  $v' = 3$  are only about one quarter of those related to  $v' = 8$ . This amount seems to be small enough in order to use OH(3-0) as a reference in this study. Since this band and also OH(4-0) are only present in data taken with the UVES 860 nm set-up, the study of non-LTE effects is focused on the corresponding sample with 1,526 spectra (see Section 3.3.1). Despite the lower size and time coverage compared to the main sample used for the study of long-term variations in Section 4.1, it is well suited to study the solar cycle effect since it covers the maximum of cycle 23 and the subsequent deep activity minimum (see Fig. 2). For the analysis, the  $T_{\text{rot}}$  of the seven selected bands with  $v'$  from 3 to 9 were corrected

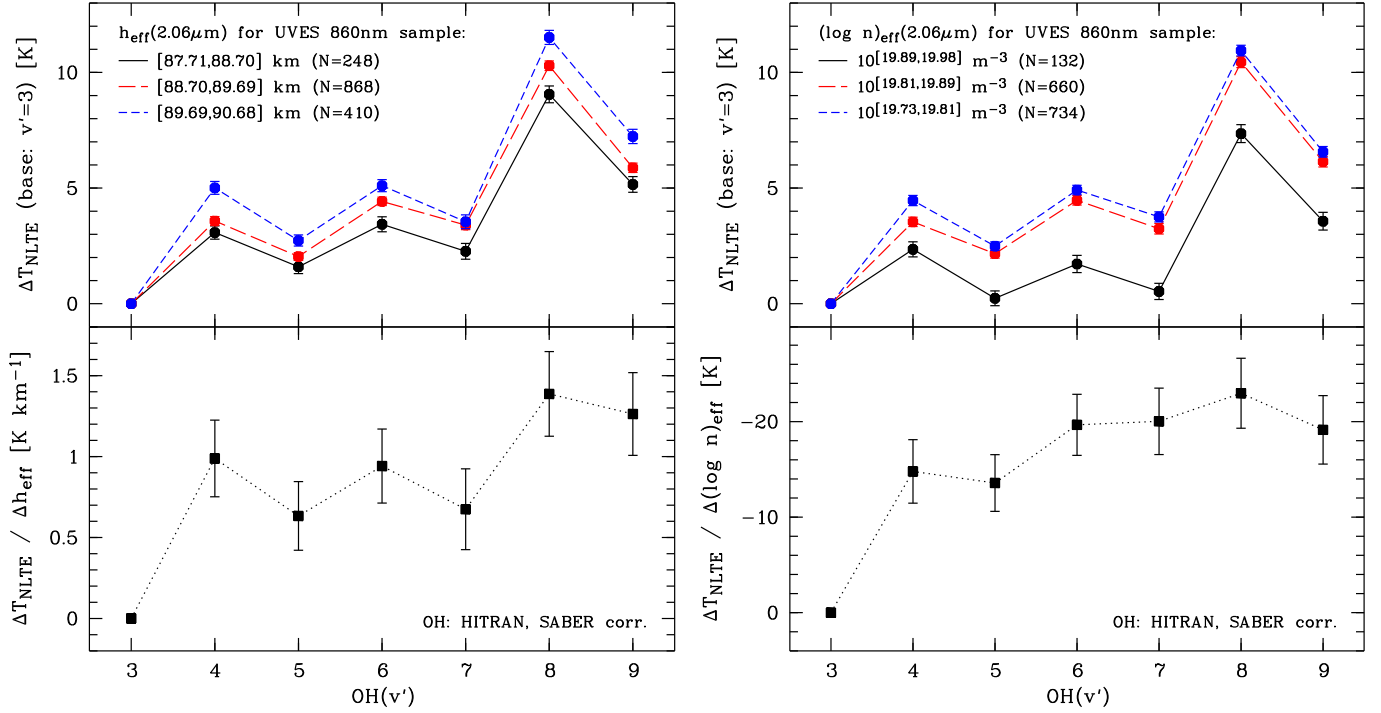


Figure 9: Change of non-LTE contributions to OH  $T_{\text{rot}}$  ( $\Delta T_{\text{NLTE}}$ ) by variations of effective height (left) and logarithmic air density (right) of the OH emission layer for the 860 nm UVES sample (see Fig. 2) and different  $v'$ . The upper panels show  $\Delta T_{\text{NLTE}}$  in K with a zero line defined by the  $T_{\text{rot}}$  for OH( $v' = 3$ ). The values for the other  $v'$  were corrected for differences in the SABER-related emission profiles and temperature offsets depending on OH band and line set (see Sect. 3.3). The  $v'$ -related  $\Delta T_{\text{NLTE}}$  are shown for three subsamples that cover the full range of effective height and logarithmic density values by intervals of equal size (see legend). The given error bars indicate the mean errors and should be considered as lower limits since the  $T_{\text{rot}}$  distribution cannot be described by a single Gaussian (see Sect. 2.1). The lower panels show the results of a linear regression analysis for the relation between  $\Delta T_{\text{NLTE}}$  and the effective height (left) and logarithmic density (right), respectively. The error bars are related to the uncertainties of the regression analysis. Note that the ordinate for the right plot is reversed in order to consider that height and density are anti-correlated. For the same reason, the order of the intervals used in the upper panels is different.

for constant offsets related to systematic measurement errors (see Section 3.3.1). Moreover, we corrected the  $T_{\text{rot}}$  for  $T_{\text{kin}}$  differences caused by the  $v'$  dependence of the OH emission height using  $v' = 3$  as the reference. This was performed by means of SABER  $T_{\text{eff}}$  data, which were linked with the UVES observations as described in Section 3.3.2. The latter was also done for the effective emission height  $h_{\text{eff}}$  and the VER-weighted decadal logarithm of the number density of air molecules in  $\text{m}^{-3}$ ,  $(\log n)_{\text{eff}}$ .

At first, we checked whether we can confirm that the contribution of non-LTE effects to OH  $T_{\text{rot}}$  depends on  $h_{\text{eff}}$ . For this purpose, we primarily used the  $h_{\text{eff}}$  values for the SABER OH channel centred on  $2.06 \mu\text{m}$  since the effective  $v'$  of about 8.3 better represents those OH bands where the largest effect is expected. Nevertheless, we tested the other OH channel as well. The results agree within the errors. The  $h_{\text{eff}}$  for the  $2.06 \mu\text{m}$  channel vary from 87.7 to 90.7 km. Note that this variation is smaller than for individual SABER profiles since the connection with UVES data was only possible by an averaging procedure (see Section 3.3.2). We divided this range in three intervals of equal size with 248, 868, and 410 UVES spec-

tra. The bin with the lowest  $h_{\text{eff}}$  therefore exhibits the highest statistical uncertainties. The  $\Delta T_{\text{NLTE}}$  results for the three intervals are given as a function of  $v'$  in Fig. 9. The values for  $v' = 3$  are always at zero since it is the reference for the calculation of the non-LTE effects. The curves for the three  $h_{\text{eff}}$  ranges convincingly confirm the expected trend. Higher  $\Delta T_{\text{NLTE}}$  are related to higher  $h_{\text{eff}}$ .

We also performed a linear regression analysis for these two parameters and the individual UVES measurements. The results can also be found in Fig. 9. The  $h_{\text{eff}}$  dependence of  $\Delta T_{\text{NLTE}}$  varies from 0.63 K per km for  $v' = 5$  to 1.39 K per km for  $v' = 8$ . With an average mean error of 0.24 K per km, all regression slopes appear to be significant except those for  $v' = 5$  and 7. There is no clear dependence on  $v'$ . However, there seems to be a weak positive correlation between the slope and  $\Delta T_{\text{NLTE}}$ , i.e. those bands which show strong non-LTE effects in  $T_{\text{rot}}$  on average are also those which tend to be more sensitive to changes in the OH emission height. Note that the significance of our results is also affected by the sample selection. As described for our main sample in Section 2.1.2, we also performed the whole analysis based on a more restrictive



data set with 1,386 spectra. This selection reduced the regression slopes in Fig. 9 by 0.27 K per km on average, which is about the mean uncertainty of the regression analysis. This result suggests that the true total uncertainties are somewhat higher. They cannot be neglected as it was possible for the analysis of the main sample of 3,113 spectra.

We also checked whether the combination of individual measurements ( $T_{\text{rot}}$ ) and weighted averages ( $T_{\text{eff}}$ ,  $h_{\text{eff}}$ ) could affect our regression results. For this purpose, we first derived averages for these quantities from the individual UVES and SABER measurements for the fixed grid of observing times and days of year discussed in Section 3.2.1. Then, the  $\Delta T_{\text{NLTE}}$  were calculated and the regression analysis was performed for the nighttime grid points. This procedure resulted in regression slopes which were slightly but not significantly lower, which justifies our approach used for Fig. 9. Nevertheless, the derived regression slopes should be taken with caution since geographical and temporal mismatches of the UVES and SABER data and the limited vertical resolution of the SABER profiles could still cause additional systematics.

The thermalisation of the OH rotational level populations essentially depends on collisions with  $\text{N}_2$  and  $\text{O}_2$  (e.g. Dodd et al., 1994; Kliner and Farrow, 1999). Therefore, the effective air density in the OH emission layer appears to be an even more promising tracer of  $\Delta T_{\text{NLTE}}$  than  $h_{\text{eff}}$ . Therefore, we performed the same analysis for  $(\log n)_{\text{eff}}$ . The logarithm of the density was chosen since it results in weights of the different parts of the emission layer which are comparable to those for the altitude. It also avoids that the most critical heights for the non-LTE contributions have negligible weight. Fig. 9 shows the results for three  $(\log n)_{\text{eff}}$  bins with 132, 660, and 734 spectra. Observations at high density are relatively rare. Since  $\Delta T_{\text{NLTE}}$  tends to increase during the night at Cerro Paranal (Noll et al., 2016), the high-density spectra are usually related to the early evening. The mean local time is 19:57. The non-LTE contributions are remarkably low for this subsample.  $\Delta T_{\text{NLTE}}$  of several Kelvins are only present for  $v' = 8$  and 9, i.e. the levels which are directly populated by the hydrogen–ozone reaction. For the other two bins, the  $\Delta T_{\text{NLTE}}$  are distinctly higher. The mean difference for the lowest and highest density intervals is 2.9 K if the results for  $v'$  from 4 to 9 are averaged. The corresponding mean difference for  $h_{\text{eff}}$  is only 1.8 K. These values confirm our assumption that  $(\log n)_{\text{eff}}$  is the better tracer for  $\Delta T_{\text{NLTE}}$ .

This can also be seen for the results of the corresponding regression analysis, which are also displayed in Fig. 9. The slopes are highly significant with an average confidence of  $5.4\sigma$ . The differences between the  $v'$ -dependent data points are relatively small and not significant. Compared to the mean value of  $-18.4\text{ K}$ , the scatter is only 3.5 K. The characteristic  $\Delta T_{\text{NLTE}}(v')$  structure is only marginally present. The large step from the reference  $v'$  of 3 to 4 challenges the assumption of comparably small  $\Delta T_{\text{NLTE}}$

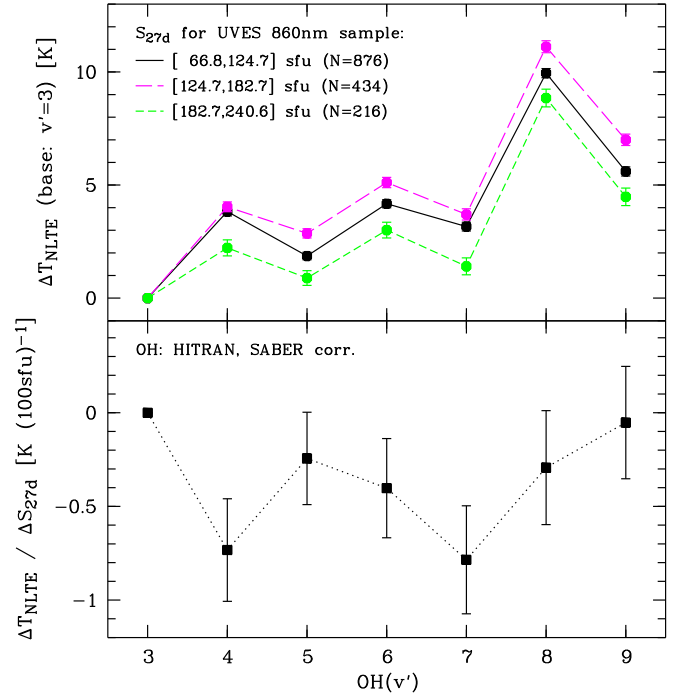


Figure 10: Change of non-LTE contributions to OH  $T_{\text{rot}}$  ( $\Delta T_{\text{NLTE}}$ ) by variations of the solar radio flux  $S_{27d}$  for the 860 nm UVES sample and different  $v'$ . For more details, see the legend and Fig. 9.

variations for the lowest  $v'$ . It might be that a significant fraction of the total effect could not be detected. The differences in the band-specific line sets used for this study (especially OH(3-0) with five and OH(4-0) with four lines, and only three common emissions; see Noll et al., 2015) might also play a role if each OH line shows a different sensitivity to non-LTE effects. If the SABER OH channel with  $v' \approx 4.6$  is used for the analysis, the result is very similar to the one for  $v' \approx 8.3$  except for a less negative mean slope of  $-15.2\text{ K}$ . The difference can be almost fully explained by a higher variability in  $(\log n)_{\text{eff}}$ . For the SABER high- $v'$  channel, the study of the alternative UVES sample with 1,386 spectra also gives a mean slope of  $-15.2\text{ K}$ . Its significance is  $4.6\sigma$ . Therefore, the sample selection uncertainty does not critically decrease the reliability of our result on the existence of strong variations of the  $T_{\text{rot}}$  non-LTE effects as a function of the effective air density. Finally, as already found for  $h_{\text{eff}}$ , the regression slopes do not appear to significantly depend on our approach for linking the SABER with the UVES data.

#### 4.3.2. Non-LTE long-term variations

The discussion in the previous section has shown that changes in the OH emission layer can cause variations in OH  $T_{\text{rot}}$  of the order of several Kelvins. This seems to be especially critical for time scales of hours to months (Noll et al., 2016). Now, the crucial question is: how large is the impact of non-LTE effects on the observed  $T_{\text{rot}}$  long-term variations? For this, we studied the dependence of

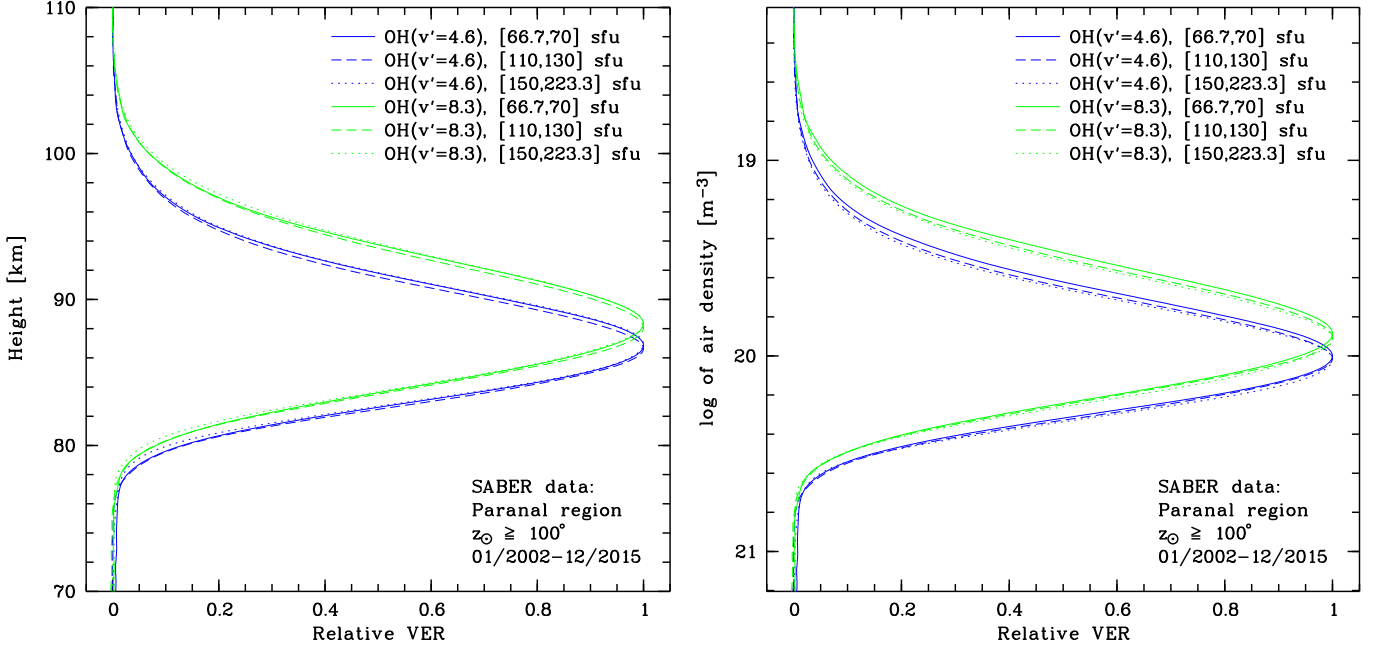


Figure 11: OH relative volume emission rate profiles of the two SABER OH channels centred on  $1.64$  ( $v' \approx 4.6$ ; blue) and  $2.06 \mu\text{m}$  ( $v' \approx 8.3$ ; green) for Cerro Paranal-related SABER subsamples with low ( $< 70$  sfu;  $N = 495$ ; solid), intermediate (between 110 and 130 sfu;  $N = 918$ ; dashed), and high ( $> 150$  sfu;  $N = 455$ ; dotted) solar radio flux  $S_{27d}$ . The profiles are shown for height (left) and logarithmic air density (right).

$\Delta T_{\text{NLTE}}$  on the solar radio flux measured by  $S_{27d}$ . We performed the same analysis as described in Section 4.3.1 for  $h_{\text{eff}}$  and  $(\log n)_{\text{eff}}$ .

The results for our UVES 860 nm sample are given in Fig. 10. The  $T_{\text{rot}}$  data set was divided into three subsamples with 876, 434, 216 members, which cover  $S_{27d}$  intervals of equal size in the range from 66.8 to 240.6 sfu. The smallest population is found for  $S_{27d}$  greater than 182.7 sfu, which only occurred during the maximum of solar cycle 23. The shape of the three  $\Delta T_{\text{NLTE}}(v')$  functions is relatively similar. However, the dependence of the non-LTE effects on  $S_{27d}$  is remarkable. The highest solar fluxes cause the lowest  $\Delta T_{\text{NLTE}}$ , whereas data taken at intermediate  $S_{27d}$  indicates the strongest non-LTE contributions. This result is inconsistent with a linear relation. Therefore, a linear regression does not seem to be well suited to describe the data. Nevertheless, we also show the results of such an analysis in Fig. 10. The slopes range from  $-0.79$  to  $-0.05$  K per 100 sfu with a mean value and error of  $-0.42 \pm 0.28$  K per 100 sfu. Using the alternative sample with 1,386 instead of 1,526 spectra, we obtain  $-0.19 \pm 0.27$  K per 100 sfu, which is even closer to zero. These results suggest that non-LTE effects seem to be almost negligible for the interpretation of the total effect of  $+4.7 \pm 0.4$  K per 100 sfu discussed in Section 4.1. However, the real situation is more complex. If we only use the data in the two intervals with the lowest  $S_{27d}$ , the regression analysis returns a mean slope of  $+0.8 \pm 0.4$  K per 100 sfu. For the two intervals with the highest  $S_{27d}$ , the

corresponding result is  $-3.5 \pm 0.7$  K per 100 sfu. Although these results should be taken with care since the involved samples are relatively small and the regression analysis is less robust, the large discrepancies in the slopes imply that the contribution of non-LTE effects could significantly depend on the sample properties. They could be an explanation for the sample-specific differences in the solar cycle effects discussed in Section 4.1.

In view of the uncertainties in the interpretation of the relation between  $\Delta T_{\text{NLTE}}$  and the solar radio flux, we also investigated the  $S_{27d}$  dependence of the OH emission profile. For this purpose, we used our SABER sample with 4,496 profiles (Section 2.2) and derived mean profiles for the two OH channels in three very different  $S_{27d}$  ranges with mean values of 68, 120, and 169 sfu. All profiles for solar fluxes below 70 sfu ( $N = 495$ ), between 110 to 130 sfu ( $N = 918$ ), and above 150 sfu ( $N = 455$ ) were considered. The resulting relative VER profiles are shown in Fig. 11 as a function of the altitude and  $\log n$ . The profiles for  $v' \approx 4.6$  and 8.3 with sample-averaged  $h_{\text{eff}}$  of 87.8 and 89.2 km show only a weak variation of a few  $10^{-1}$  km and  $10^{-2}$  logarithmic units. The profile for the highest solar activity shows the highest effective emission height and density. This apparent contradiction can be explained by an expansion of the atmosphere which is stronger than the rise of the OH emission layer. The expansion is expected due to the warming effect (see Sect. 4.1) by the increased solar energy input at high solar activity. This effect becomes especially strong at higher altitudes in the thermo-

sphere (e.g. Emmert et al., 2010). Fig. 11 also suggests that the response of the OH emission layer on the solar activity is not a linear function since the profile for intermediate  $S_{27d}$  is the lowest in terms of altitude. Another aspect of the weak profile variations is the corresponding negligible change in the  $T_{\text{kin}}$ -related  $T_{\text{eff}}$ . For the mean OH VER and  $T_{\text{kin}}$  profile of our SABER sample, the sensitivity is only about  $-0.2$  K per km.

In order to better understand the effect of the solar cycle on the full SABER sample, we performed a linear regression analysis for  $h_{\text{eff}}$  and  $(\log n)_{\text{eff}}$  similar to the ones for the SABER-related OH intensities and temperatures (Section 3.2.3). The  $h_{\text{eff}}$ -related slopes for the solar cycle effect are  $0.00 \pm 0.06$  and  $+0.07 \pm 0.05$  km per 100 sfu for the channels related to  $v' \approx 4.6$  and 8.3. This is not significant. The linear long-term trend also turned out to be consistent with zero. For  $(\log n)_{\text{eff}}$ , there could be a weak negative trend as indicated by a mean value of  $-0.007 \pm 0.003$  per decade for both OH channels. The solar cycle sensitivity is more significant but still weak. We derived  $+0.019 \pm 0.004$  and  $+0.016 \pm 0.004$  per 100 sfu for the channels related to  $v' \approx 4.6$  and 8.3. Hence, there is a positive correlation of  $(\log n)_{\text{eff}}$  and  $S_{27d}$ , as already suggested by Fig. 11.

As described in Section 4.2.2, Gao et al. (2016) also used SABER data to study long-term variations in the OH emission. This analysis included a latitude-dependent regression analysis for the peak height of the emission in both channels. They did not find any significant effect, which we can confirm based on an analysis also using the emission peak. As illustrated by Fig. 11, changes due to high solar activity appear to be limited to the faint wings of the emission profile, which cannot be measured by the peak height and where also  $h_{\text{eff}}$  does not seem to be sensitive enough. Based on OH(3-1) VER profiles from SCIAMACHY on Envisat, von Savigny (2015) performed a regression analysis for the long-term trends in  $h_{\text{eff}}$  for the years 2003 to 2011, 22:00 local solar time, and several  $10^\circ$  latitude bins. Linear trends are negligible. Only for the range from  $20$  to  $30^\circ$  N, there could be a weak trend of  $-0.26 \pm 0.07$  km per decade. There is no significant solar cycle effect in the investigated latitude range from  $10^\circ$  S to  $30^\circ$  N. For the range from  $20$  to  $30^\circ$  N, the result is  $+0.19 \pm 0.13$  km per 100 sfu, which agrees well with our findings. Finally, Liu and Shepherd (2006) used OH(8-3) VER profiles related to WINDII onboard UARS to investigate the peak emission altitude for the years from 1991 to 1997 for several latitude intervals. For  $20$  to  $30^\circ$  S, they found a significant slope of about  $+1.4$  km per 100 sfu. It is not clear how this large deviation from the other results can be explained (von Savigny, 2015).

As a final alternative estimation of the contributions of varying non-LTE effects to the OH  $T_{\text{rot}}$  long-term variations, we can combine the slopes for  $\Delta T_{\text{NLTE}}$  versus  $h_{\text{eff}}$  or  $(\log n)_{\text{eff}}$  (see Section 4.3.1) with those for  $h_{\text{eff}}$  or  $(\log n)_{\text{eff}}$  versus  $S_{27d}$ . The resulting amounts can be considered as lower limits for the solar cycle effect since a single parameter like  $h_{\text{eff}}$  cannot trace all variations related to the impact

of the solar activity on the OH  $T_{\text{rot}}$ . As input for the slopes that were derived from our UVES 860 nm sample, we used the  $v'$ -averaged mean values, i.e.  $+0.98 \pm 0.24$  K per km and  $-18.4 \pm 3.4$  K for the SABER  $2.06 \mu\text{m}$  OH channel data and  $+0.94 \pm 0.21$  K per km and  $-15.2 \pm 2.8$  K for the  $1.64 \mu\text{m}$  data. These slopes were then multiplied by the corresponding ones for the  $h_{\text{eff}}$  and  $(\log n)_{\text{eff}}$  solar cycle effects listed above. In the end, we obtained four estimates which range from  $-0.35$  to  $+0.07$  K per 100 sfu. The most negative value is related to  $(\log n)_{\text{eff}}$  and  $v' \approx 8.3$ . The average of the four slopes is  $-0.13 \pm 0.12$  K per 100 sfu. For completeness, we also performed this calculation for the long-term trend, which resulted in  $+0.06 \pm 0.06$  K per decade and is extremely small. These results suggest that the long-term variations of OH  $T_{\text{rot}}$  at Cerro Paranal for 2000 to 2015 are only slightly affected by non-LTE effects. The same conclusion can be drawn from the comparison of the UVES  $T_{\text{rot}}$  and SABER  $T_{\text{eff}}$  trends in Section 4.1 and the direct regression analysis for  $\Delta T_{\text{NLTE}}$  and  $S_{27d}$ . The main reason for this behaviour appears to be the long-term stability of the OH emission layer.

## 5. Conclusions

We used 3,113 spectra from the UVES echelle spectrograph at the VLT in Chile to study the long-term variations in OH intensity and OH-related rotational temperature  $T_{\text{rot}}$  for the period from April 2000 to March 2015. Focusing on the strongest P-branch lines of the five OH bands (5-1), (6-2), (7-3), (8-3), and (9-4), our linear regression analysis resulted in a strong solar cycle effect in both parameters, which does not significantly depend on the vibrational level of the upper state  $v'$ . The mean effect for all bands is  $+16.1 \pm 1.9\%$  per 100 sfu for the relative intensity and  $+4.7 \pm 0.4$  K per 100 sfu for  $T_{\text{rot}}$ . We do not see significant long-term trends.

For a comparison, we also analysed 4,496 nighttime limb-sounding observations of the multi-channel radiometer SABER on TIMED for the Cerro Paranal region and the period from January 2002 to December 2015. The vertically-integrated volume emission rates (VERs) for the two OH-related channels with effective  $v' \approx 4.6$  and 8.3 showed a mean solar cycle effect of  $+13.3 \pm 1.9\%$  per 100 sfu. In the case of the VER-weighted kinetic temperature profiles, we obtained an effect of  $+4.3 \pm 0.4$  K per 100 sfu. There is no significant  $v'$  dependence and the corresponding long-term trends are consistent with zero. Our UVES- and SABER-related trend parameters agree well with each other. Other results from the literature for SABER data and ground-based OH measurements at low and mid-latitudes are generally consistent with our findings. For the few long OH  $T_{\text{rot}}$  time series at low latitudes, we could even find that the agreement appears to be much better than previously expected from the published values, which mainly deviate by differences in the analysis and limitations in the data sets.

Measurements of kinetic temperatures in the mesopause region by means of OH  $T_{\text{rot}}$  are affected by varying contributions of non-LTE effects  $\Delta T_{\text{NLTE}}$ . They are caused by variations in the frequency of the crucial thermalising OH collisions with air molecules compared to radiative processes and deactivating or destructing collisions with atomic oxygen. They can be estimated by comparisons of  $T_{\text{rot}}$  with large  $v'$  differences corrected for deviations in the OH emission profiles. We studied their impact on the long-term variations by different approaches.

The small difference in the temperatures from UVES and SABER data is already a good indication that the non-LTE contributions must be low. A regression analysis for  $\Delta T_{\text{NLTE}}$  and the solar radio flux for a sample of 1,526 UVES spectra where the OH bands (3-0) and (4-0) could also be measured revealed a mean solar cycle effect for all  $v'$  from 4 to 9 of  $-0.4 \pm 0.3$  K per 100 sfu. A more indirect approach included an intermediate step involving the  $\Delta T_{\text{NLTE}}$  dependence on the SABER-related effective emission height  $h_{\text{eff}}$  and the effective decadal logarithm of the air density for the emission layer  $(\log n)_{\text{eff}}$ , which are good indicators for the change of the non-LTE effects. This is demonstrated by  $v'$ -averaged  $\Delta T_{\text{NLTE}}$  sensitivities for  $h_{\text{eff}}$  and  $(\log n)_{\text{eff}}$  from the two SABER OH channels of  $+1.0 \pm 0.2$  K per km and  $-17 \pm 3$  K relative to a reference  $v'$  of 3. Using the relation between  $h_{\text{eff}}$  or  $(\log n)_{\text{eff}}$  and the solar radio flux for both SABER OH channels and the full sample, the resulting mean solar cycle effect for  $\Delta T_{\text{NLTE}}$  is  $-0.1 \pm 0.1$  K, which agrees with our other estimates. This approach also provides a result for the long-term term trend, which is consistent with zero. The small contribution of non-LTE effects to the solar cycle variability is caused by only weak long-term variations of the OH emission profile, which is in accordance with other studies. The negative sign in our estimates for the non-LTE effects seems to be related to an increase in the air density in the OH emission layer for higher solar activity.

Our results show that  $\Delta T_{\text{NLTE}}$  contributions to OH  $T_{\text{rot}}$ , which can be critical on shorter time scales, do not appear to significantly affect the strong solar cycle effects found in our data. This is good news for studies of  $T_{\text{rot}}$  long-term variations. The global application of our findings depends on the stability of the OH emission layer. So far, the corresponding results are promising. Our study also shows that it is necessary to cover a sufficiently long period with a wide range of solar activity levels. Otherwise significant systematic deviations could be found for the total effect as well as the non-LTE contributions. In part, this might be related to non-linearities in the response of the OH emission layer to solar forcing.

## Acknowledgments

This project made use of the ESO Science Archive Facility. UVES Phase 3 spectra from different observing programmes of the period from April 2000 to March 2015 were analysed. We thank the SABER team for providing

the data products used in this paper. Moreover, we thank the two anonymous referees for their detailed and very helpful comments. S. Noll receives and B. Proxauf and S. Unterguggenberger received funding from the project P26130 of the Austrian Science Fund (FWF). W. Kausch was funded by the project IS538003 (Hochschulraumstrukturmittel) provided by the Austrian Ministry for Research (BMWFV).

## References

- Adler-Golden, S., 1997. Kinetic parameters for OH nightglow modeling consistent with recent laboratory measurements. *J. Geophys. Res.* 102, 19969–19976. doi:10.1029/97JA01622.
- Baker, D.J., Stair, Jr., A.T., 1988. Rocket measurements of the altitude distributions of the hydroxyl airglow. *Phys. Scripta* 37, 611–622. doi:10.1088/0031-8949/37/4/021.
- Bates, D.R., Nicolet, M., 1950. The Photochemistry of Atmospheric Water Vapor. *J. Geophys. Res.* 55, 301–327. doi:10.1029/JZ055i003p00301.
- Beig, G., 2011a. Long-term trends in the temperature of the mesosphere/lower thermosphere region: 1. Anthropogenic influences. *J. Geophys. Res.* 116, A00H11. doi:10.1029/2011JA016646.
- Beig, G., 2011b. Long-term trends in the temperature of the mesosphere/lower thermosphere region: 2. Solar response. *J. Geophys. Res.* 116, A00H12. doi:10.1029/2011JA016766.
- Beig, G., Keckhut, P., Lowe, R.P., Roble, R.G., Mlynczak, M.G., Scheer, J., Fomichev, V.I., Offermann, D., French, W.J.R., Shephard, M.G., Semenov, A.I., Remsberg, E.E., She, C.Y., Lübken, F.J., Bremer, J., Clemesha, B.R., Stegman, J., Sigernes, F., Fadnavis, S., 2003. Review of mesospheric temperature trends. *Rev. Geophys.* 41, RG1015. doi:10.1029/2002RG000121.
- Beig, G., Scheer, J., Mlynczak, M.G., Keckhut, P., 2008. Overview of the temperature response in the mesosphere and lower thermosphere to solar activity. *Rev. Geophys.* 46, RG3002. doi:10.1029/2007RG000236.
- Brooke, J.S.A., Bernath, P.F., Western, C.M., Sneden, C., Afşar, M., Li, G., Gordon, I.E., 2016. Line strengths of rovibrational and rotational transitions in the X<sup>2</sup>Π ground state of OH. *J. Quant. Spectrosc. Radiat. Transf.* 168, 142–157. doi:10.1016/j.jqsrt.2015.07.021.
- Clemesha, B., Takahashi, H., Simonich, D., Gobbi, D., Batista, P., 2005. Experimental evidence for solar cycle and long-term change in the low-latitude MLT region. *J. Atmos. Sol.-Terr. Physics* 67, 191–196. doi:10.1016/j.jastp.2004.07.027.
- Clough, S.A., Shephard, M.W., Mlawer, E.J., Delamere, J.S., Iacono, M.J., Cady-Pereira, K., Boukabara, S., Brown, P.D., 2005. Atmospheric radiative transfer modeling: a summary of the AER codes. *J. Quant. Spectrosc. Radiat. Transf.* 91, 233–244. doi:10.1016/j.jqsrt.2004.05.058.
- Cosby, P.C., Sharpee, B.D., Slanger, T.G., Huestis, D.L., Hanuschik, R.W., 2006. High-resolution terrestrial nightglow emission line atlas from UVES/VLT: Positions, intensities, and identifications for 2808 lines at 314–1043 nm. *J. Geophys. Res.* 111, A12307. doi:10.1029/2006JA012023.
- Cosby, P.C., Slanger, T.G., 2007. OH spectroscopy and chemistry investigated with astronomical sky spectra. *Can. J. Phys.* 85, 77–99. doi:10.1139/P06-088.
- Dekker, H., D’Odorico, S., Kaufer, A., Delabre, B., Kotzłowski, H., 2000. Design, construction, and performance of UVES, the echelle spectrograph for the UT2 Kueyen Telescope at the ESO Paranal Observatory, in: Iye, M., Moorwood, A.F. (Eds.), *Optical and IR Telescope Instrumentation and Detectors*, pp. 534–545. doi:10.1117/12.395512.
- Dodd, J.A., Armstrong, P.S., Lipson, S.J., Lowell, J.R., Blumberg, W.A.M., Nadile, R.M., Adler-Golden, S.M., Marinelli, W.J., Holtzclaw, K.W., Green, B.D., 1994. Analysis of hydroxyl earthlimb airglow emissions: Kinetic model for state-to-

- state dynamics of OH( $v$ ,N). *J. Geophys. Res.* 99, 3559–3586. doi:10.1029/93JD03338.
- Dudok de Wit, T., Kretzschmar, M., Abouadarham, J., Amblard, P.O., Auchère, F., Liliensten, J., 2008. Which solar EUV indices are best for reconstructing the solar EUV irradiance? *Adv. Space Res.* 42, 903–911. doi:10.1016/j.asr.2007.04.019.
- Dudok de Wit, T., Kretzschmar, M., Liliensten, J., Woods, T., 2009. Finding the best proxies for the solar UV irradiance. *Geophys. Res. Lett.* 36, L10107. doi:10.1029/2009GL037825.
- Emmert, J.T., Lean, J.L., Picone, J.M., 2010. Record-low thermospheric density during the 2008 solar minimum. *Geophys. Res. Lett.* 37, L12102. doi:10.1029/2010GL043671.
- Gao, H., Xu, J., Chen, G.M., 2016. The responses of the nightglow emissions observed by the TIMED/SABER satellite to solar radiation. *J. Geophys. Res.* 121, 1627–1642. doi:10.1002/2015JA021624.
- Gelinas, L.J., Hecht, J.H., Walterscheid, R.L., Roble, R.G., Woithe, J.M., 2008. A seasonal study of mesospheric temperatures and emission intensities at Adelaide and Alice Springs. *J. Geophys. Res.* 113, A01304. doi:10.1029/2007JA012587.
- Goldman, A., Schoenfeld, W.G., Goorvitch, D., Chackerian, Jr., C., Dothe, H., Mélen, F., Abrams, M.C., Selby, J.E.A., 1998. Updated line parameters for OH  $X^2\Pi-X^2\Pi$  ( $v',v''$ ) transitions. *J. Quant. Spectrosc. Radiat. Transf.* 59, 453–469. doi:10.1016/S0022-4073(97)00112-X.
- Hamuy, M., Suntzeff, N.B., Heathcote, S.R., Walker, A.R., Gigoux, P., Phillips, M.M., 1994. Southern spectrophotometric standards, 2. *Publ. Astron. Soc. Pac.* 106, 566–589. doi:10.1086/133417.
- Hanuschik, R.W., 2003. A flux-calibrated, high-resolution atlas of optical sky emission from UVES. *Astron. Astrophys.* 407, 1157–1164. doi:10.1051/0004-6361/20030885.
- Huang, F.T., Mayr, H.G., Russell, III, J.M., Mlynczak, M.G., 2016. Ozone and temperature decadal responses to solar variability in the stratosphere and lower mesosphere, based on measurements from SABER on TIMED. *Ann. Geophys.* 34, 801–813. doi:10.5194/angeo-34-801-2016.
- Kalichinsky, C., Knieling, P., Koppmann, R., Offermann, D., Steinbrecht, W., Wintel, J., 2016. Long-term dynamics of OH\* temperatures over central Europe: trends and solar correlations. *Atmos. Chem. Phys.* 16, 15033–15047. doi:10.5194/acp-16-15033-2016.
- Kalogerakis, K.S., Matsiev, D., Sharma, R.D., Wintersteiner, P.P., 2016. Resolving the mesospheric nighttime 4.3  $\mu\text{m}$  emission puzzle: Laboratory demonstration of new mechanism for OH( $v$ ) relaxation. *Geophys. Res. Lett.* 43, 8835–8843. doi:10.1002/2016GL069645.
- Kausch, W., Noll, S., Smette, A., Kimeswenger, S., Barden, M., Szyszka, C., Jones, A.M., Sana, H., Horst, H., Kerber, F., 2015. Molecfit: A general tool for telluric absorption correction. II. Quantitative evaluation on ESO-VLT/X-Shooter spectra. *Astron. Astrophys.* 576, A78. doi:10.1051/0004-6361/201423909.
- Khomich, V.Y., Semenov, A.I., Shefov, N.N., 2008. Airglow as an Indicator of Upper Atmospheric Structure and Dynamics. Springer, Berlin.
- Kliner, D.A.V., Farrow, R.L., 1999. Measurements of ground-state OH rotational energy-transfer rates. *J. Chem. Phys.* 110, 412–422. doi:10.1063/1.478073.
- Liu, G., Shepherd, G.G., 2006. An empirical model for the altitude of the OH nightglow emission. *Geophys. Res. Lett.* 33, L09805. doi:10.1029/2005GL025297.
- Liu, W., Xu, J., Smith, A.K., Yuan, W., 2015. Comparison of rotational temperature derived from ground-based OH airglow observations with TIMED/SABER to evaluate the Einstein coefficients. *J. Geophys. Res.* 120, 10,069–10,082. doi:10.1002/2015JA021886.
- Meinel, I.A.B., 1950. OH Emission Bands in the Spectrum of the Night Sky. *Astrophys. J.* 111, 555. doi:10.1086/145296.
- Mies, F.H., 1974. Calculated vibrational transition probabilities of OH( $X^2\Pi$ ). *J. Molec. Spectrosc.* 53, 150–188. doi:10.1016/0022-2852(74)90125-8.
- Moehler, S., Modigliani, A., Freudling, W., Giammichele, N., Gianninas, A., Gonneau, A., Kausch, W., Lançon, A., Noll, S., Rauch, T., Vinther, J., 2014. Flux calibration of medium-resolution spectra from 300 nm to 2500 nm: Model reference spectra and telluric correction. *Astron. Astrophys.* 568, A9. doi:10.1051/0004-6361/201423790.
- Nath, O., Sridharan, S., 2014. Long-term variabilities and tendencies in zonal mean TIMED-SABER ozone and temperature in the middle atmosphere at 10–15°N. *J. Atmos. Sol.-Terr. Phys.* 120, 1–8. doi:10.1016/j.jastp.2014.08.010.
- Noll, S., Kausch, W., Barden, M., Jones, A.M., Szyszka, C., Kimeswenger, S., Vinther, J., 2012. An atmospheric radiation model for Cerro Paranal. I. The optical spectral range. *Astron. Astrophys.* 543, A92. doi:10.1051/0004-6361/201219040.
- Noll, S., Kausch, W., Kimeswenger, S., Unterguggenberger, S., Jones, A.M., 2015. OH populations and temperatures from simultaneous spectroscopic observations of 25 bands. *Atmos. Chem. Phys.* 15, 3647–3669. doi:10.5194/acp-15-3647-2015.
- Noll, S., Kausch, W., Kimeswenger, S., Unterguggenberger, S., Jones, A.M., 2016. Comparison of VLT/X-shooter OH and O<sub>2</sub> rotational temperatures with consideration of TIMED/SABER emission and temperature profiles. *Atmos. Chem. Phys.* 16, 5021–5042. doi:10.5194/acp-16-5021-2016.
- Parihar, N., Singh, D., Gurubaran, S., 2017. A comparison of ground-based hydroxyl airglow temperatures with SABER/TIMED measurements over 23° N, India. *Ann. Geophys.* 35, 353–363. doi:10.5194/angeo-35-353-2017.
- Pendleton, Jr., W.R., Taylor, M.J., 2002. The impact of L-uncoupling on Einstein coefficients for the OH Meinel (6,2) band: implications for Q-branch rotational temperatures. *J. Atmos. Sol.-Terr. Phys.* 64, 971–983. doi:10.1016/S1364-6826(02)00051-2.
- Pertsev, N., Perminov, V., 2008. Response of the mesopause airglow to solar activity inferred from measurements at Zvenigorod, Russia. *Ann. Geophys.* 26, 1049–1056. doi:10.5194/angeo-26-1049-2008.
- Reid, I.M., Spargo, A.J., Woithe, J.M., 2014. Seasonal variations of the nighttime O(<sup>1</sup>S) and OH(8-3) airglow intensity at Adelaide, Australia. *J. Geophys. Res.* 119, 6991–7013. doi:10.1002/2013JD020906.
- Reisin, E.R., Scheer, J., 2002. Evidence of change after 2001 in the seasonal behaviour of the mesopause region from airglow data at El Leoncito. *Adv. Space Res.* 44, 401–412. doi:10.1016/j.asr.2009.04.007.
- Reisin, E.R., Scheer, J., Dyrland, M.E., Sigernes, F., Deehr, C.S., Schmidt, C., Höppner, K., Bittner, M., Ammosov, P.P., Gavrilyeva, G.A., Stegman, J., Perminov, V.I., Semenov, A.I., Knieling, P., Koppmann, R., Shiokawa, K., Lowe, R.P., López-González, M.J., Rodríguez, E., Zhao, Y., Taylor, M.J., Buriti, R.A., Espy, P.J., French, W.J.R., Eichmann, K.U., Burrows, J.P., von Savigny, C., 2014. Traveling planetary wave activity from mesopause region airglow temperatures determined by the Network for the Detection of Mesospheric Change (NDMC). *J. Atmos. Sol.-Terr. Phys.* 119, 71–82. doi:10.1016/j.jastp.2014.07.002.
- Rezac, L., Kutepov, A., Russell, III, J.M., Feofilov, A.G., Yue, J., Goldberg, R.A., 2015. Simultaneous retrieval of T(p) and CO<sub>2</sub> VMR from two-channel non-LTE limb radiances and application to daytime SABER/TIMED measurements. *J. Atmos. Sol.-Terr. Phys.* 130, 23–42. doi:10.1016/j.jastp.2015.05.004.
- Rothman, L.S., Gordon, I.E., Babikov, Y., Barbe, A., Chris Benner, D., Bernath, P.F., Birk, M., Bizzocchi, L., Boudon, V., Brown, L.R., Campargue, A., Chance, K., Cohen, E.A., Coudert, L.H., Devi, V.M., Drouin, B.J., Fayt, A., Flaud, J.M., Gamache, R.R., Harrison, J.J., Hartmann, J.M., Hill, C., Hodges, J.T., Jacquemart, D., Jolly, A., Lamouroux, J., Le Roy, R.J., Li, G., Long, D.A., Lyulin, O.M., Mackie, C.J., Massie, S.T., Mikhailenko, S., Müller, H.S.P., Naumenko, O.V., Nikitin, A.V., Orphal, J., Perevalov, V., Perrin, A., Polovtseva, E.R., Richard, C., Smith, M.A.H., Starikova, E., Sung, K., Tashkun, S., Tennyson, J., Toon, G.C., Tyuterev, V.G., Wagner, G., 2013. The HITRAN2012 molecular spectroscopic database. *J. Quant. Spectrosc. Radiat. Transf.* 130, 4–50. doi:10.1016/j.jqsrt.2013.07.002.
- Rousselot, P., Lidman, C., Cuby, J.G., Moreels, G., Monnet, G., 2000. Night-sky spectral atlas of OH emission lines in the near-infrared. *Astron. Astrophys.* 354, 1134–1150.

- Rozenberg, G.V., 1966. *Twilight: a Study in Atmospheric Optics*. Plenum Press, New York.
- Russell, III, J.M., Mlynczak, M.G., Gordley, L.L., Tansock, J., Esplin, R., 1999. Overview of the SABER experiment and preliminary calibration results, in: Larar, A.M. (Ed.), *Optical Spectroscopic Techniques and Instrumentation for Atmospheric and Space Research III*, pp. 277–288. doi:10.1117/12.366382.
- Scheer, J., Reisin, E.R., 2013. Simpson's paradox in trend analysis: An example from El Leoncito airglow data. *J. Geophys. Res.* 118, 5223–5229. doi:10.1002/jgra.50461.
- Scheer, J., Reisin, E.R., Mandrini, C.H., 2005. Solar activity signatures in mesopause region temperatures and atomic oxygen related airglow brightness at El Leoncito, Argentina. *J. Atmos. Sol.-Terr. Phys.* 67, 145–154. doi:10.1016/j.jastp.2004.07.023.
- Schmidt, C., Höppner, K., Bittner, M., 2013. A ground-based spectrometer equipped with an InGaAs array for routine observations of OH(3-1) rotational temperatures in the mesopause region. *J. Atmos. Sol.-Terr. Phys.* 102, 125–139. doi:10.1016/j.jastp.2013.05.001.
- Smette, A., Sana, H., Noll, S., Horst, H., Kausch, W., Kimeswenger, S., Barden, M., Szyszka, C., Jones, A.M., Gallenne, A., Vinther, J., Ballester, P., Taylor, J., 2015. Molecfit: A general tool for telluric absorption correction. I. Method and application to ESO instruments. *Astron. Astrophys.* 576, A77. doi:10.1051/0004-6361/201423932.
- Takahashi, H., Clemesha, B.R., Batista, P.P., 1995. Predominant semi-annual oscillation of the upper mesospheric airglow intensities and temperatures in the equatorial region. *J. Atmos. Terr. Phys.* 57, 407–414. doi:10.1016/0021-9169(94)E0006-9.
- Takahashi, H., Gobbi, D., Batista, P.P., Melo, S.M.L., Teixeira, N.R., Buriti, R.A., 1998. Dynamical influence on the equatorial airglow observed from the south american sector. *Adv. Space Res.* 21, 817–825. doi:10.1016/S0273-1177(97)00680-7.
- Tapping, K.F., 2013. The 10.7 cm solar radio flux ( $F_{10.7}$ ). *Space Weather* 11, 394–406. doi:10.1002/swe.20064.
- Tüg, H., 1977. Vertical Extinction on La Silla. *The Messenger* 11, 7–8. URL: <https://www.eso.org/sci/publications/messenger/archive/no.11-dec77/messenger-no11.pdf>.
- van Rhijn, P.J., 1921. On the brightness of the sky at night and the total amount of starlight. *Publ. Kapteyn Astron. Lab. Groningen* 31, 1–83.
- Vernet, J., Dekker, H., D'Odorico, S., Kaper, L., Kjaergaard, P., Hammer, F., Randich, S., Zerbi, F., Groot, P.J., Hjorth, J., Guinouard, I., Navarro, R., Adolfse, T., Albers, P.W., Amans, J.P., Andersen, J.J., Andersen, M.I., Binetruy, P., Bristow, P., Castillo, R., Chemla, F., Christensen, L., Conconi, P., Conzelmann, R., Dam, J., de Caprio, V., de Ugarte Postigo, A., Delabre, B., di Marcantonio, P., Downing, M., Elswijk, E., Finger, G., Fischer, G., Flores, H., François, P., Goldoni, P., Guglielmi, L., Haigron, R., Hanenburg, H., Hendriks, I., Horrobin, M., Horville, D., Jessen, N.C., Kerber, F., Kern, L., Kiekebusch, M., Kleszcz, P., Klougart, J., Kragt, J., Larsen, H.H., Lizon, J.L., Lucuix, C., Mainieri, V., Manuputy, R., Martayan, C., Mason, E., Mazzoleni, R., Michaelsen, N., Modigliani, A., Moehler, S., Møller, P., Norup Sørensen, A., Nørregaard, P., Péroux, C., Patat, F., Pena, E., Pragt, J., Reinero, C., Rigal, F., Riva, M., Roelfsema, R., Royer, F., Sacco, G., Santin, P., Schoenmaker, T., Spano, P., Sweers, E., Ter Horst, R., Tintori, M., Tromp, N., van Dael, P., van der Vliet, H., Venema, L., Vidali, M., Vinther, J., Vola, P., Winters, R., Wistisen, D., Wulterkens, G., Zacchei, A., 2011. X-shooter, the new wide band intermediate resolution spectrograph at the ESO Very Large Telescope. *Astron. Astrophys.* 536, A105. doi:10.1051/0004-6361/201117752.
- von Savigny, C., 2015. Variability of OH(3-1) emission altitude from 2003 to 2011: Long-term stability and universality of the emission rate-altitude relationship. *J. Atmos. Sol.-Terr. Phys.* 127, 120–128. doi:10.1016/j.jastp.2015.02.001.
- von Savigny, C., McDade, I.C., Eichmann, K.U., Burrows, J.P., 2012. On the dependence of the OH\* Meinel emission altitude on vibrational level: SCIAMACHY observations and model simulations. *Atmos. Chem. Phys.* 12, 8813–8828. doi:10.5194/acp-12-8813-2012.
- Wintoft, P., 2011. The variability of solar EUV: A multiscale comparison between sunspot number, 10.7 cm flux, LASP MgII index, and SOHO/SEM EUV flux. *J. Atmos. Sol.-Terr. Phys.* 73, 1708–1714. doi:10.1016/j.jastp.2011.03.009.
- Xu, J., Gao, H., Smith, A.K., Zhu, Y., 2012. Using TIMED/SABER nightglow observations to investigate hydroxyl emission mechanisms in the mesopause region. *J. Geophys. Res.* 117, D02301. doi:10.1029/2011JD016342.